Mechanisms of energetic-particle transport in magnetically confined plasmas

Cite as: Phys. Plasmas **27**, 030901 (2020); https://doi.org/10.1063/1.5136237
Submitted: 11 November 2019 • Accepted: 01 January 2020 • Published Online: 02 March 2020

W. W. Heidbrink and R. B. White

Physics of Plasmas TUTORIAL scitation.org/journal/php

Mechanisms of energetic-particle transport in magnetically confined plasmas

Cite as: Phys. Plasmas **27**, 030901 (2020); doi: 10.1063/1.5136237
Submitted: 11 November 2019 · Accepted: 1 January 2020 ·
Published Online: 2 March 2020

W. W. Heidbrink[1,a),b)] and R. B. White[2]

AFFILIATIONS

[1]University of California, Irvine, California 92697, USA
[2]Princeton Plasma Physics Laboratory, Princeton, New Jersey 08543, USA

Note: This paper is part of the Special Collection: Papers from the 61st Annual Meeting of the APS Division of Plasma Physics.
Note: Paper UT3 1, Bull. Am. Phys. Soc. **64** (2019).
[a)]Invited speaker.
[b)]**Author to whom correspondence should be addressed:** Bill.Heidbrink@uci.edu

ABSTRACT

Super-thermal ions and electrons occur in both space and fusion plasmas. Because these energetic particles (EP) have large velocities, EP orbits necessarily deviate substantially from magnetic surfaces. Orbits are described by conserved constants of motion that define topological boundaries for different orbit types. Electric and magnetic field perturbations produced by instabilities can disrupt particle orbits, causing the constants of motion to change. The statistics of the "kicks" associated with these perturbations determines the resulting cross field transport. A unifying theme of this tutorial is the importance of the perturbation's phase at the particle's position $\Theta = \mathbf{k}\cdot\mathbf{r} - \omega t$, where k and ω are the wavevector and frequency of the perturbation, r is the EP position, and t is the time. A distinction is made between field perturbations that resonate with an aspect of the orbital motion and those that do not. Resonance occurs when the wave phase returns to its initial value in an integer multiple of an orbital period. Convective transport occurs when resonant particles experience an unvarying wave phase. Alternatively, multiple wave-particle resonances usually decorrelate the phase, resulting in diffusive transport. Large orbits increase the number of important resonances and can cause chaotic orbits even for relatively small amplitude waves. In contrast, in the case of non-resonant perturbations, orbital phase averaging reduces transport. Large field perturbations introduce additional effects, including nonlinear resonances at fractional values of the orbital motion. In summary, large orbits are a blessing and a curse: For non-resonant modes, orbit-averaging reduces transport but, for resonant transport, large orbits facilitate jumps across topological boundaries and enhance the number of important resonances.

I. INTRODUCTION

Superthermal particles occur frequently in both natural and laboratory plasmas. Although all plasma particles are energetic by ordinary standards, in this tutorial, an "energetic particle" (EP) has two properties: (1) the energy is substantially greater than the bulk plasma temperature and (2) Coulomb collisions cause negligible deflections on the timescale of a single orbit in the confining magnetic field. In nature, EPs are produced when a rapidly drifting plasma merges with a colder plasma, for example, when the solar wind collides with the magnetosphere. Instabilities that accelerate ions or electrons to high energies are another common source in natural plasmas. In fusion plasmas, there are four common sources. Because Coulomb drag decreases with energy, a DC electric field that is parallel to the magnetic field can create "runaway" electrons that continuously gain energy if the electric field acceleration exceeds Coulomb drag. For ions, injection of energetic neutral beams is one important source. Acceleration by radio frequency waves at the fundamental ion cyclotron frequency or its harmonics is a second important source of fast ions. Charged fusion reaction products, such as the ^{4}He alpha particles created by deuterium–tritium reactions, are the third important source of fast ions in fusion plasmas.

All of these EPs share common properties that distinguish them from thermal plasma. The distribution function of a thermal species is described by a Maxwellian, possibly a drifting Maxwellian or a Maxwellian with small distortions. As a result, fluid equations derived by taking velocity moments of the underlying kinetic equations are a sensible starting point for transport theory. This is not the case for EPs. Because the energies are high and EP densities are generally low,

inter-species EP collisions are rare. Consequently, EP distribution functions have complicated dependencies on energy and direction. Because different EP velocities behave quite differently, a single-particle picture is the appropriate starting point for EP transport theory.

The purpose of this review is to introduce the key ideas of single-particle transport theory for EPs. Many of these mechanisms also apply to thermal particles but they are particularly important for EPs. The review is tutorial in nature, not comprehensive. No attempt is made to cite the first or most seminal work on a particular topic, or to reference every relevant paper. Rather, examples are selected for their clarity.

Detailed discussion of the instabilities that cause transport is beyond the scope of this review. From the perspective adopted here, DC electromagnetic fields $\mathbf{E}_0$ and $\mathbf{B}_0$ govern the unperturbed equilibrium EP orbits. An instability produces electric and magnetic fields $\mathbf{E}_1$ and $\mathbf{B}_1$ that perturb the orbits. Static perturbations associated with field errors or an additional field coil can also be considered a perturbing field. The perturbing fields have different frequency, spatial structure, and polarization but, regardless of origin, they may cause EP transport.

The perturbing fields cause transport in both velocity space and configuration space. For magnetic fusion, cross field spatial transport is of paramount concern but, for this review, motion in any phase-space direction is considered "transport."

Calculation of the EP distribution function is also outside the scope. The focus here is on processes that alter EP orbits on a relatively short timescale. On a longer timescale, the distribution function is shaped by sources, sinks, collisions, and the wave-particle interactions considered here. A Fokker–Planck equation is often used to describe these processes. Well-known examples of fast-ion distribution functions derived from Fokker-Planck equations can be found in Ref. 1 for neutral-beam injection and in Ref. 2 for EP tails created by RF acceleration. Although Coulomb and other collisions play important roles in shaping the distribution function, they are only briefly discussed here (Sec. III B). Another barely discussed topic is calculation of "prompt losses" (losses that occur in the first full orbit of an EP in a confinement device). More details on all of these topics appear in Secs. 3 and 4.1 of Ref. 3.

The important topic of diagnostic techniques that enable measurements of EP transport is also omitted.

The review begins with a discussion of equilibrium orbits, particularly their description using constants-of-motion and the importance of topological boundaries (Sec. II). Section III introduces the general framework for considering the effect of field perturbations, including the distinction between reversible and irreversible motion. Criteria for modification of a constant-of-motion are given. Section IV is about the wave-particle phase and the distinction between resonant and non-resonant perturbations. For non-resonant particles, orbit averaging dramatically reduces cross field transport (Sec. V). Section VI discusses the convective transport that occurs when a resonant particle stays in phase with the perturbing field. Multiple resonances cause stochastic diffusive transport (Sec. VII). Large perturbations introduce new effects, including fractional resonances (Sec. VIII).

II. EQUILIBRIUM ORBITS

We assume the existence of equilibrium electromagnetic fields that (in the absence of perturbations and collisions) confine EPs in much of phase space. The confining fields may be electric, magnetic, or both, for simplicity, consider magnetic confinement. The magnetic configuration could have open field lines (as in a solenoid), or be a toroidal system where the field lines trace out two-dimensional flux surfaces (as in an axisymmetric tokamak), or be a fully three dimensional toroidal system with regions without well-defined flux surfaces (as in a stellarator). The orbital motion consists of relatively fast gyromotion superimposed upon a drifting guiding center. Gyromotion is described by the magnitude of the perpendicular velocity $v_\perp$ and the rapidly varying gyroangle; the velocity vector of the drift orbit is described by $v_\parallel$ (the component of the velocity parallel to $\mathbf{B}_0$) and the perpendicular drift $\mathbf{v}_d$. The "pitch" of the orbit is $v_\parallel/v$.

Because of the perpendicular drifts, to confine particles, magnetic field lines in toroidal geometries must twist toroidally as they advance poloidally, a property called "rotational transform."[4]

Different timescales describe different aspects of the orbital motion. In all magnetic configurations, the gyromotion sets the fastest timescale, occurring at the gyrofrequency ω_c. In toroidal systems, two other frequencies describe periodicities of the drift orbit. One of these describes the frequency of motion in the toroidal direction ω_ϕ; the other describes the frequency of motion in the poloidal direction ω_θ. Normally the ratio of these periods is irrational, so the orbit covers a two dimensional drift surface; it is not periodic. A prototypical orbit is the orbit of a charged particle in a dipole field, representative of orbits in the radiation belts (Fig. 1). For this orbit, the fastest motion is the gyromotion at ω_c, followed by the north–south motion at bounce

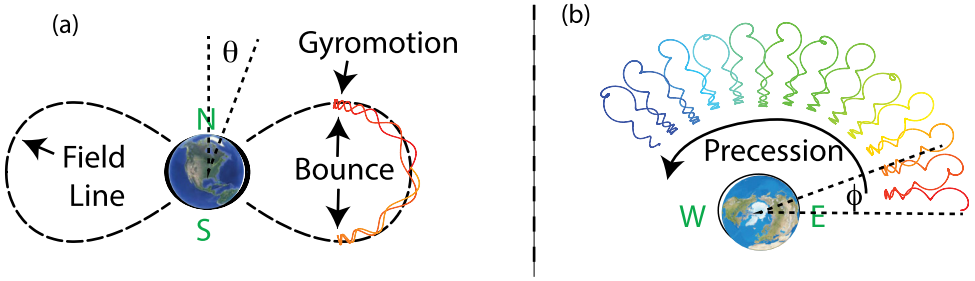

FIG. 1. Energetic orbit in a dipole field (dashed line). (a) Projection onto the (r, z) plane. The transverse gyromotion, vertical bounce motion, and poloidal angle θ are indicated. (b) View of the orbit from above the North pole, showing the slower azimuthal precessional drift in the toroidal ϕ direction. In both projections, a rainbow color scale (from red through violet) indicates advancing time.

frequency ω_θ, followed by the east–west precession around the earth at frequency ω_ϕ.

In all systems, EPs deviate farther from field lines than thermal particles. This occurs for two reasons. First, since the gyroradius is proportional to $v_\perp$, the EP gyroradius is larger than the gyroradius of thermal particles of the same species. The difference is also great for the drift orbit. The gradient-B drift is (Sec. 3.1 of Ref. 5)

$$\mathbf{v}_{\nabla B} = \frac{W_\perp}{q}\frac{\mathbf{B}\times\nabla B}{B^3}, \tag{1}$$

where $W_\perp = \frac{1}{2}mv_\perp^2$ is the perpendicular energy and q is the charge. The curvature drift is (Sec. 3.2 of Ref. 5)

$$\mathbf{v}_{curv} = \frac{2W_\parallel}{qB^2}\frac{\mathbf{R}_c\times\mathbf{B}}{R_c^2}, \tag{2}$$

where $W_\parallel = \frac{1}{2}mv_\parallel^2$ and $\mathbf{R}_c$ is the radius of field-line curvature. Evidently, both these cross field drifts are proportional to energy. Consequently, the deviation of an EP guiding-center orbit from a flux surface is often an order of magnitude larger than for thermal particles.

The large deviations have two important consequences. First, unlike for thermal particles, an orbit cannot be meaningfully linked to one particular field line or flux surface in the plasma. As a result, EP orbits are most efficiently described by their constants-of-motion (Sec. II A).

The second consequence concerns orbit classification. Orbit classification is also useful for thermal particles. Perhaps the most familiar example is a magnetic mirror. In a mirror device, particles with sufficiently large $v_\perp/v$ reflect off the high-field region in the mirror throat and remain confined but particles with low values of $v_\perp/v$ escape

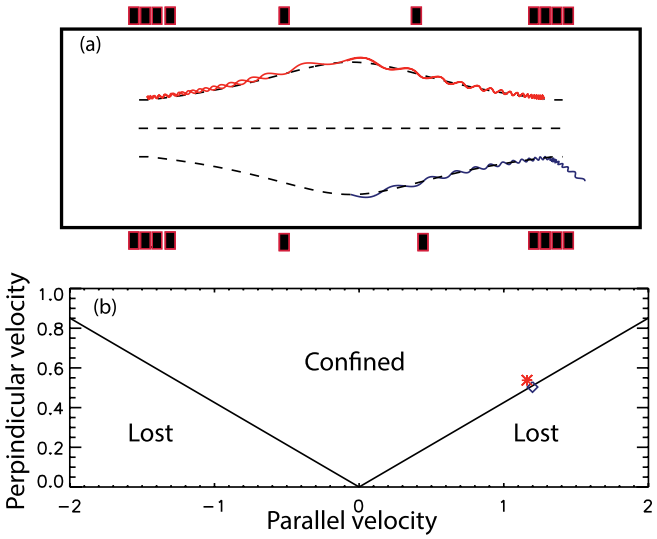

FIG. 2. (a) Examples of lost (blue) and confined (red) orbits in a simple magnetic mirror of mirror ratio $B_{max}/B_{min} = 5$. Dashed lines represent magnetic field lines. (b) Topological map in velocity space at the center of the mirror, indicating the boundary between confined and lost particles. The location of the confined orbit in the upper figure is indicated by the red asterisk; the blue diamond indicates the location of the illustrated loss orbit.

[Fig. 2(a)]. In $(v_\parallel, v_\perp)$ velocity space, there is a boundary that separates the "loss cone" from the confinement region [Fig. 2(b)]. In a tokamak, a similar $(v_\parallel, v_\perp)$ boundary separates "passing" particles that circulate in a single direction toroidally around the device from "trapped" (also called "banana") orbits that reverse toroidal direction due to mirror trapping in regions of high magnetic field. Similar topological boundaries occur for EPs but, for them, the large drifts create new orbit types that do not exist for thermal particles. Orbit classification and topological boundaries are discussed in Sec. II B.

A. Constants of motion

A complete description of any orbit is given by its position $\mathbf{r}$ and velocity $\mathbf{v}$ as a function of time. Although accurate, this description requires six coordinates, three for velocity space and three for configuration space. Identification of invariants of the motion reduces the number of coordinates needed for unique designation of a particular orbit. These invariants are of two types: exact invariants and adiabatic invariants.

Because collisions are negligible on the timescale of an orbit, the energy is an exact invariant of the equilibrium orbit. If a cross field electric potential Φ exists, the conserved energy is the sum of the kinetic energy and the electrostatic potential energy. Since the potential energy is often much smaller than the kinetic energy for EPs, often the kinetic energy alone can be considered the conserved quantity. If there is a component of the electric field parallel to $\mathbf{B}_0$, the particle will accelerate and change energy. This happens, for example, with runaway electrons in a tokamak but typically the energy gained in a single orbit is $O(10^{-6})$ of the kinetic energy; so parallel acceleration can be neglected in the orbital description.

Energy conservation is associated with reversibility in time. Using Noether's theorem, other symmetries also have associated exact invariants. For example, in a solenoid or symmetric mirror machine, the canonical azimuthal angular momentum is an exact invariant; in an axisymmetric toroidal device like an ideal tokamak or field-reversed configuration (FRC), the canonical toroidal angular momentum is an exact invariant of the motion. This invariant is $P_\phi = mrv_\phi + qrA_\phi$, where m and q are the mass and charge of the EP, r is the radius, ϕ is the azimuthal or toroidal angle, and A_ϕ is the azimuthal or toroidal component of the magnetic vector potential. In a toroidal device, P_ϕ is often written as

$$P_\phi = mrv_\phi + q\Psi_p, \tag{3}$$

where $\Psi_p = rA_\phi$ is the poloidal flux.

In classical mechanics, adiabatic invariants are associated with the quantity known as the "action," $J_i = \oint P_i\, dQ_i$, where P_i is a canonical momentum, Q_i is a generalized coordinate, and the integral is over a periodic motion. The theory of adiabatic invariants asserts that the action is a constant of the motion when certain conditions that are described in Sec. III C are satisfied, even if the system is gradually changing. For charged particle motion in a magnetic field, the fastest periodic motion is the gyromotion. The associated adiabatic invariant is designated as the first adiabatic invariant μ, where

$$\mu = \frac{W_\perp}{B}. \tag{4}$$

The first adiabatic invariant is denoted by μ because it is proportional to the diamagnetic magnetic moment of the charged particle as it

orbits in the magnetic field. In configurations where the magnetic field strength varies across the gyroradius or the particle drifts in an electric field, additional terms appear in the definition of μ.[6,7] The relativistic adiabatic invariant that corresponds to μ is given in Eq. (2) of Ref. 8.

The first adiabatic invariant is associated with perpendicular gyromotion. The second adiabatic invariant is associated with motion parallel to the field and is given by

$$J_2 = \oint v_\parallel ds, \tag{5}$$

where the integral is over periodic motion along a field line. For example, for a particle in the earth's dipole field, J_2 is associated with the vertical bounce motion illustrated in Fig. 1(a).

The third adiabatic invariant is associated with cross field drifts such as the precession around the earth illustrated in Fig. 1(b). The full expression for J_3 includes a contribution from the mechanical momentum but it is often the case that v_d is sufficiently small that the magnetic contribution to the canonical momentum dominates. In that case, J_3 is proportional to the magnetic flux enclosed by the precessing orbit.

Exact and adiabatic invariants are not necessarily independent. For example, in an axisymmetric torus, the toroidal canonical angular momentum P_ϕ is related to the third adiabatic invariant J_3.

Once an invariant of the motion has been identified (whether exact or adiabatic), it can be used to reduce the dimensionality of the system. For example, the constancy of μ implies that the gyrophase does not impact the trajectory of the orbit. Neglecting the gyrophase reduces the six coordinates needed to describe arbitrary motion to five coordinates. Axisymmetry in a mirror device implies that the azimuthal angle is an ignorable coordinate that does not influence the orbital trajectory.

For example, in an axisymmetric tokamak, three quantities are constant: energy, magnetic moment, and toroidal canonical angular momentum. These three quantities are often used to enumerate the possible orbits. An advantage of these coordinates is that, in the presence of perturbations, a relationship often holds between changes in energy and changes in momentum; see Sec. IV. On the other hand, for numerical work, other coordinates are more convenient. (The toroidal canonical angular momentum is multi-valued depending on the sign of v_ϕ so a fourth coordinate is needed.) One convenient set of coordinates is the energy, the maximum major radius of the orbit, and the value of $v_\parallel/v$ at the maximum radius.

In other configurations, other coordinates are favored. However, in all configurations, it is advisable to utilize constants-of-motion to reduce the dimensionality of the system.

B. Orbit classification and topological boundaries

The existence of two different orbit types and the corresponding topological map that separates them has already been illustrated for a simple magnetic mirror (Fig. 2). Other configurations have their own orbit types and topological maps. Figure 3 shows examples for tokamak and FRC geometry. Owing to the large drifts, EP orbits exist that have no counterpart for thermal particles. Consider the tokamak. For low-energy thermal particles, there are three orbit types: co-passing, trapped, and counter-passing. (Here, co- and counter-passing refer to the toroidal direction of the circulating particles with respect to the plasma current.) These also exist for EPs but there are also new orbit types [Figs. 3(a) and 3(b)]. One of these is a "loss" orbit that collides with the wall. Another is a "stagnation" orbit. A stagnation orbit circulates toroidally around the torus while scarcely moving poloidally. The phenomenon occurs because, for an EP, the poloidal component of parallel motion along the field line can be canceled by the vertical grad-B and curvature drifts. (This cancelation can also occur for a thermal particle but only in a negligibly small portion of phase space.) Additional non-standard orbits exist for EPs as well (Sec. 3.3 of Refs. 9 and 10).

Important orbit types in an FRC are "drift," "figure-8," and "betatron" orbits [Fig. 3(c)]. Figure-8 and betatron orbits exist because the large orbit sample regions of quite different magnetic field. The corresponding topological map is shown in Fig. 3(d). More details of FRC orbits can be found in Refs. 11 and 12.

Three dimensional stellarator configurations support even more orbit types for both thermal and energetic particles. One important example is a "super-banana" that becomes helically trapped between regions of high magnetic-field strength; this prevents the particle from precessing around the torus. This phenomenon also occurs in realistic tokamaks because the finite number of toroidal field coils causes "ripple" in the toroidal field that breaks the toroidal symmetry. In describing stellarator orbits and topology, convenient variables are energy, μ, and J^*, the latter being a generalized version of the second adiabatic invariant.[13]

The existence of topological boundaries has important implications for EP transport. If a Coulomb collision or field perturbation causes an EP to cross a topological boundary, the particle can take a large transport step. An example is shown for a tokamak in Fig. 3(a). The difference in velocity between the illustrated "counter-passing" orbit and the "lost" orbit is very slight ($\Delta v_\parallel/v < 0.3\%$) but one orbit is well confined and the other hits the wall. Measurements with loss detectors often measure loss orbits near a topological boundary (Fig. 4). In this example, measurements of the velocity vector of the lost particles at the detector enable the experimenters to follow the lost orbit backward in time in the equilibrium fields. The observed losses correspond to an orbit that is at the boundary between counter-passing and lost orbits.

The equilibrium orbits shown in Fig. 3(a) illustrate a general feature of orbits in magnetic configurations: Orbits that circulate parallel to the plasma current are better confined than orbits that circulate opposite to the plasma current. In Fig. 3(a), for all three illustrated orbits, there is a location along the orbit where the vertical grad-B and curvature drifts nearly cancel the vertical component of the parallel drift v_θ. For the stagnation orbit, this cancelation occurs outside of the magnetic axis; for the counter-passing and lost orbits, this near-cancelation occurs inside of the magnetic axis. The two points of exact cancelation are very different, however.[15] For the stagnation orbit, the exact cancelation occurs at an "O-point" in orbit topology space, so nearby orbits satisfy an elliptic equation and are well confined. For the counter-passing and lost orbits, the exact cancellation occurs at an "X-point" in orbit topology space, so nearby orbits satisfy a hyperbolic equation and deviate rapidly from the equilibrium point. ("O-points" and "X-points" in orbit phase space are illustrated in Sec. IV B.) Similar phenomena occur in other magnetic configurations. Modeling of a cylindrical astrophysical current-carrying jet shows that co-current orbits satisfy elliptic equations, while countercurrent orbits satisfy hyperbolic equations and are poorly confined.[16] Even in stellarators where the current is carried by external conductors, beam ions

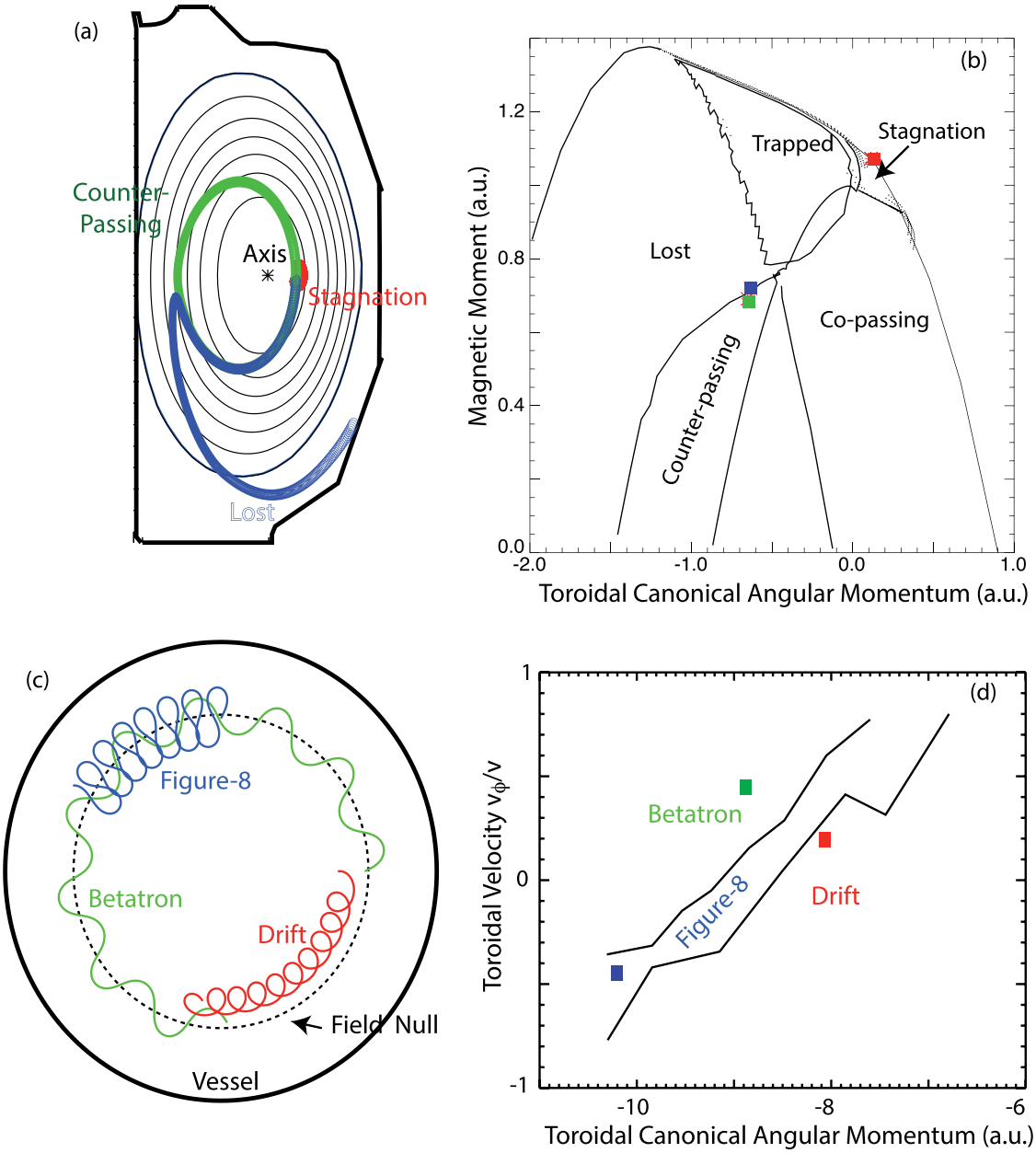

FIG. 3. Examples of different orbit types in (a) a tokamak and in (c) an FRC. The tokamak orbits have been projected onto the (r, z) plane and the FRC orbits are projected onto the (r, ϕ) plane. Corresponding topological map for (b) tokamak and (d) FRC orbits. In both cases, the energy is fixed, the abscissa is proportional to the canonical toroidal angular momentum, and the three orbits shown in the left panels are marked by colored squares. In (b), the ordinate is proportional to the magnetic moment; in (d), the ordinate is the toroidal velocity component v_ϕ/v at the midplane. The tokamak example uses a DIII-D equilibrium; the FRC example uses an analytical FRC equilibrium, the Hill's vortex.[11]

injected in the co-current direction are better confined than beam ions injected in the countercurrent direction.

C. Stochasticity

In analyzing magnetic field topology and particle orbits, one often draws phase-space maps called Poincare (or puncture) plots. These are made by plotting positions in phase space at regular intervals. For example, in tracing a magnetic field line in toroidal geometry, one can plot the (r, z) position of the field line every time it passes a particular toroidal angle. Figure 5 shows an example for two configurations in the W7-X stellarator.

In Poincare plots, a distinction is made between quasi-periodic and chaotic trajectories. In Fig. 5, field lines in the plasma interior

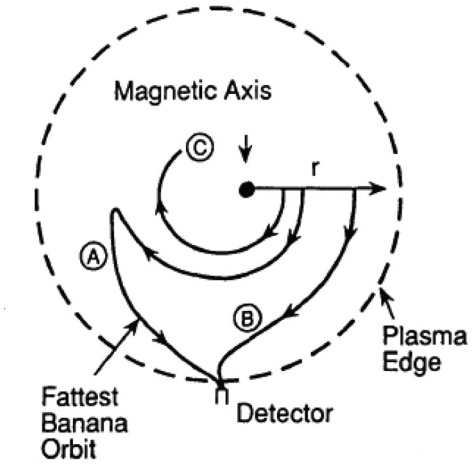

FIG. 4. Projection of three guiding center orbits for 1 MeV tritons in the TFTR tokamak. The dashed line represents the edge of the plasma and the loss detector is at the bottom of the tokamak. Orbit B is a measured orbit with large magnetic moment that is far from the loss boundary. Orbit A is the measured loss orbit that is at the loss boundary. It has the same energy and μ as the confined counter-passing orbit C. If orbit C diffuses outward slightly, it crosses the loss boundary and is detected. Adapted with permission from Zweben *et al.*, Nucl. Fusion **31**, 2219 (1991).[14] Copyright 1991 International Atomic Energy Agency.

always remain on the same two-dimensional surface and are on quasi-periodic trajectories. (If the Poincare plot is tracing field lines, these are the flux surfaces.) In contrast, under some conditions, traced field lines with nearly identical initial conditions diverge exponentially, even though the underlying **B**-field equations are deterministic. The field lines in the upper region of the plasma in Fig. 5 are stochastic. (Except near the edge, stochastic field lines are an undesirable property in a magnetic confinement device.) When a stochastic orbit is traced in a Poincare plot, it wanders ergodically throughout the stochastic region. Regions with stochastic trajectories are often limited by Kolmogorov–Arnold–Moser (KAM)[18] surfaces of quasi-periodic orbits that prevent a stochastic field line from wandering through all of phase space.

Poincare plots play an important role in the analysis of EP orbits (Sec. IV E).

Although in common parlance "chaotic" and "stochastic" orbits are often used interchangeably, there is a technical distinction between "chaos" and "stochasticity." Strictly speaking, stochastic motion is random at all times and distances, while chaotic motion is predictable on a short timescale but appears random for longer periods. Since collisionless orbits are deterministic, when they diverge exponentially, they are properly termed chaotic.

D. On the calculation of orbits

Orbit calculations are foundational for an understanding of EP transport. Although the focus of this tutorial review is on the physics of EP transport, not diagnostic or computational techniques, a few brief remarks are appropriate here. One type of orbit calculation involves solving the Lorentz force law; these are called "full-orbit" or "particle" calculations. The disadvantage of full-orbit codes is that resolving the gyromotion usually increases the computational expense and numerical

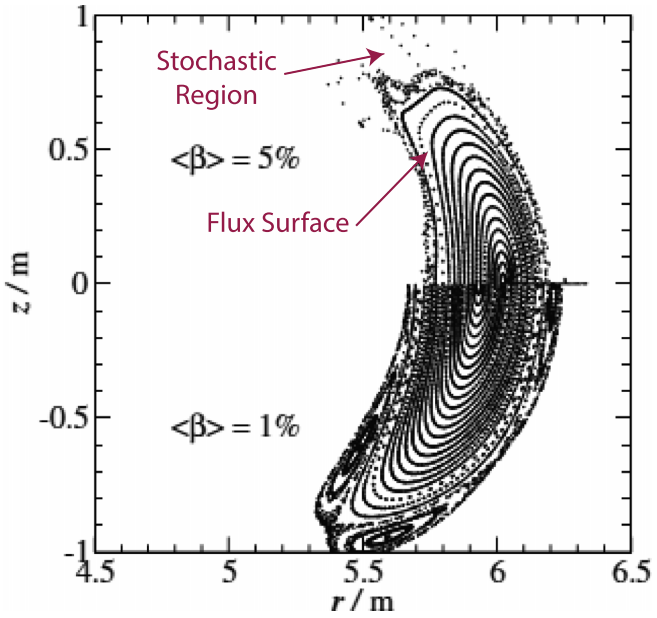

FIG. 5. Poincare plot of the equilibrium field in low-beta (lower half) and high-beta (upper half) conditions in the W7-X stellarator. The flux surfaces are the well-defined, kidney-bean shaped curves. In the high-beta configuration, the field is stochastic in the upper portion of the plasma; this is evident by the appearance of randomly scattered points. Adapted with permission from Helander *et al.*, Plasma Phys. Controlled Fusion **54**, 124009 (2012).[17] Copyright 2012 Institute of Physics Publishing.

error. In systems without high frequency perturbations where the magnetic moment is an adiabatic invariant, one can average over the cyclotron motion and maintain only the average particle motion in space. The elimination of the rapid cyclotron motion is computationally efficient. A code that follows the guiding center is a "guiding-center" code.

For example, consider a toroidal device with toroidal angle ϕ and poloidal angle θ. It is convenient to use coordinates defined by the equilibrium magnetic field, which must consist of nested toroidal surfaces, as in the core of the stellarator of Fig. 5. Let $2\pi\psi$ denote the toroidal flux contained in a flux surface with label ψ. In the guiding center approximation, the particle Hamiltonian reduces from $H = mv^2/2 + \Phi(\vec{x})$ to

$$H = mv_\parallel^2/2 + \mu B(\psi,\theta) + \Phi(\psi,\theta,\phi). \tag{6}$$

The equations of motion in Hamiltonian form are[9,19]

$$\begin{aligned} \dot{\theta} &= \frac{\partial H}{\partial P_\theta} \quad \dot{P}_\theta = -\frac{\partial H}{\partial \theta} \\ \dot{\phi} &= \frac{\partial H}{\partial P_\phi} \quad \dot{P}_\phi = -\frac{\partial H}{\partial \phi}, \end{aligned} \tag{7}$$

where the canonical momenta are expressed in magnetic coordinates [rather than the cylindrical coordinates of Eq. (3)],

$$P_\phi = g\rho_\parallel - \Psi_p, \quad P_\theta = \psi + \rho_\parallel I, \tag{8}$$

and Ψ_p is the poloidal flux, with $d\psi/d\Psi_p = q(\Psi_p)$, the field line helicity. The variable $\rho_\parallel = v_\parallel/B$ is the normalized parallel velocity and

the functions $g(\Psi_p)$ and $I(\Psi_p)$ are the toroidal and poloidal components of the magnetic field in a covariant representation,[4,9] $\mathbf{B} = g\nabla\phi + I\nabla\theta$. Toroidal symmetry implies that P_ϕ is a constant of motion, and, in this case, the three constants, energy W, magnetic moment μ, and P_ϕ (plus the sign of $v_\parallel$) completely define an orbit in the axisymmetric system.

In addition to computational speed, a Hamiltonian formalism has a further advantage. In all orbit calculations, it is important to minimize numerical errors that cause constants-of-motion to diverge from their true values. A Hamiltonian formalism has favorable conservation properties.[7] In that regard, it is also important to select a favorable numerical method, such as 4th order Runge–Kutta or an accurate symplectic integrator such as Boris integration.[20]

An advantage of EP calculations is that the dilute EPs do not interact among themselves. Consequently, efficient orbit-following codes utilize parallel processing.

III. IRREVERSIBLE TRANSPORT

This section establishes the general framework for the discussion of EP transport. Transport occurs when perturbations cause changes in the constants of motion. Section III A explains when constants-of-motion are conserved and when they are broken. Section III B explains why collisions cause minimal transport. Section III C discusses the distinction between reversible and irreversible transport and the relationship between microcsopic kicks imparted by perturbations and macroscopic transport.

A. Criteria for preservation of adiabatic invariants

The theory of adiabatic invariants is well established within classical mechanics. Within plasma physics, the monograph written by Northrop over 50 years ago[21] still provides a useful introduction and the textbook by Bellan uses pendulum motion to illustrate the key ideas.[22] To summarize, three criteria must be satisfied for an adiabatic invariant to be conserved.

(1) The orbit must experience gradual variations on the timescale of the periodic motion.
(2) The perturbations cannot resonate with a periodicity of the motion.
(3) The perturbation must be small.

These criteria are explained in more detail below.

The criterion for gradual variation is most easily explained for gyromotion. The first adiabatic invariant μ is the constant-of-motion associated with this periodicity of the orbit. The magnetic field may be changing in time, may have a gradient in space, or both. The gyrating particle "feels" these changes along its actual trajectory. The meaning of "gradual" change in time is that B changes slowly compared to a cyclotron period, i.e., $(\partial B/\partial t)/(\omega_c B) \ll 1$. The meaning of gradual change in space is that the particle experiences small changes in B as it traverses its gyro-orbit, i.e., $\rho_c \nabla B/B \ll 1$, where ρ_c is the Larmor radius. When both these conditions are satisfied, μ is conserved. In practice, in many actual calculations, these inequalities do not need to be particularly small for μ conservation to hold. (For example, 25% variations are often tolerable.)

Analogous criteria hold for the second and third adiabatic invariants.

The second general criterion is that the perturbations cannot resonate with a periodicity of the motion. This concept is easily grasped. Imagine pushing a child on a swing. If small pushes are synchronized with the natural frequency of the swing, the child gains energy. Randomly timed small pushes only yield an exasperated child! Resonance is discussed in detail in Sec. IV.

The third general criterion could be viewed as a corollary of the first but it is convenient to state it separately. Even if a perturbation is stationary in time and has a small gradient, if the amplitude is sufficiently large, it may "kick" the particle onto an entirely new orbit by displacing it into a region of altered equilibrium field.

Although there is a theoretical distinction between exact and adiabatic invariants, the distinction is unimportant in practice. For example, the toroidal canonical angular momentum is an exact invariant in an ideal tokamak but real tokamaks invariably have field errors that cause deviations from perfect axisymmetry. In practice, one still needs to know when P_ϕ is a good constant of motion and when it is not. The general criteria listed above are useful for this purpose.

As an example, consider the effect of toroidal field ripple on fast-ion confinement in a tokamak. In a real tokamak, the toroidal field is corrugated because of the finite number of toroidal field coils. From the standpoint adopted here, the toroidal field ripple is a periodic $\mathbf{B}_1$ perturbation of zero frequency. If $\mathbf{B}_1$ is sufficiently large, the invariant P_ϕ is broken.

The effect is most pronounced for trapped particles. Since $\nabla\mathbf{B}_1$ is small on the scale of the gyromotion, μ is conserved. At the turning point of a trapped ion, the parallel velocity vanishes and $\mu = W_\perp/B = W/B$. Since the energy of the particle W is another constant of the motion in static magnetic fields, small changes in the magnitude of B associated with field ripple cause perturbations in the position of the turning point. Two effects on the orbit are distinguished. The one discussed here is called "ripple trapping;" the other is called "stochastic ripple diffusion."[23] Both are explained together with many experimental examples in Sec. 4.2 of Ref. 3. An additional theoretical explanation appears in Sec. 8.7 of Ref. 9.

In ripple trapping, the toroidal field ripple creates a secondary magnetic well. An ion trapped in the secondary well executes an orbit known as a "super-banana" and begins to drift vertically because the ∇B drift is no longer compensated by rotational transform. Since EPs are collisionless, they keep drifting vertically until they are lost. Figure 6 shows an example of a lost super-banana orbit. Two tokamaks have performed experiments where the number of energized toroidal field coils was intentionally halved, thereby increasing the toroidal field ripple an order of magnitude. In both cases, large reductions in the number of confined EPs on trapped orbits were observed.[24,25]

Minimization of the number of super-bananas is a key aspect of stellarator design. A number of optimization strategies have been developed that reduce transport associated with ripple trapping.[27,28] Equilibria with superior confinement have EP orbits with large poloidal drifts but small radial drifts. Large poloidal drift velocities promote the formation of poloidally closed contours of the second adiabatic invariant J_2, resulting in better trapped-particle confinement.[29]

B. Collisions

Collisions are a key topic in the discussion of thermal transport. Coulomb collisions cause "classical" transport in a uniform

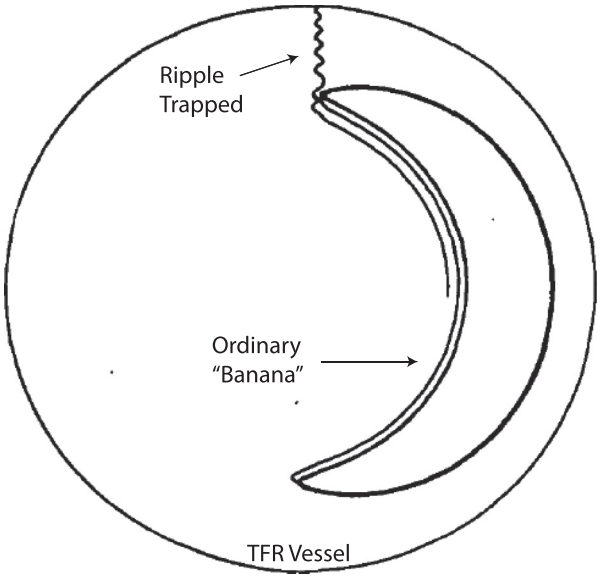

FIG. 6. Projection onto the (r, z) plane of an EP guiding center orbit in a circular cross section tokamak with ~3% toroidal field ripple. The EP initially is on an ordinary trapped-particle orbit. The small variations in the radius of the turning point are caused by small toroidal variations in B. At one helical ripple well, the orbit becomes trapped and drifts vertically to the vacuum vessel wall. Based on an experiment in the TFR tokamak. Adapted with permission from R. J. Goldston and H. H. Towner, J. Plasma Phys. **26**, 283 (1981).[26] Copyright 1981 Cambridge University Press; Authors licensed under a CCC #4716151511365.

magnetic field.[30] In magnetic confinement geometries, a finite drift-orbit width and transitions between different orbit types cause increased transport relative to classical levels; this is called "neoclassical" transport.[31] In some configurations, neoclassical transport is the dominant thermal transport mechanism, exceeding transport caused by unstable waves.

This is not the case for EPs. Because of their large velocities, collisions are rare. Appreciable transport occurs almost exclusively near topological boundaries. Near a boundary, the slight change in velocity vector associated with pitch-angle scattering can kick the EP onto an entirely different orbit, resulting in a large spatial step or even particle loss. Figures 2, 3(a), 3(b), and 4 show examples of loss orbits that differ only slightly from a confined orbit.

Figure 7 shows a concrete example for the ITER tokamak.[32] In the calculation, an orbit-following code that includes Coulomb collisions and realistic ITER fields follows alpha particles until they are lost or thermalized. Particles born in a loss region escape on their first full orbit. Particles born in a region where stochastic ripple diffusion and ripple transport are operative are lost after ~10 orbits. Away from these regions, losses are very slight; for example, over 50% of particles with a pitch within 0.1 of a boundary remain confined for thousands of orbits. Most particles are thermalized before they are scattered into a loss channel, which is why the fraction of particles lost decreases rapidly as one moves away from the loss channels. As another example, quantitatively, the neoclassical diffusion coefficient of beam ions in contemporary tokamaks is $D < 0.1$ m^2/s, which implies minimal spatial transport in a slowing-down time. Accordingly, collisionless transport is the focus of this review.

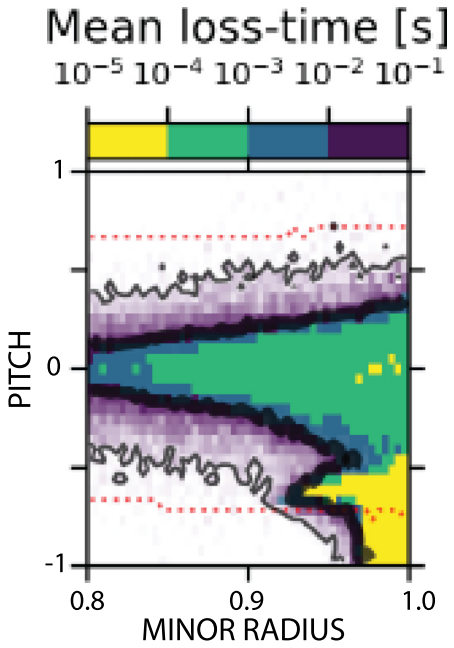

FIG. 7. Calculated loss time of 3.5 MeV alphas in an ITER plasma with toroidal field ripple. The yellow orbits that are confined $<100\ \mu$s are prompt losses. The green orbits that are confined between 0.1 and 1.0 ms are losses caused by toroidal field ripple. The purple losses are caused by Coulomb collisions. The thick (thin) black lines show where 90% (10%) of launched particles are lost. No losses are found in white regions. The coordinates are the pitch and normalized minor radius at the largest major radius of the initial orbit. The dotted red lines are the nominal trapped/passing boundary. Reproduced with permission from K. Särkimäki, Nucl. Fusion **60**, 036002 (2020).[32] Copyright 2019 the International Atomic Energy Agency.

The previous discussion concerns the dominant collisional process in fully ionized plasma, small-angle Coulomb scattering. In special circumstances, other collisional processes can be important. When measuring EPs at a pitch far from their birth pitch, large-angle nuclear scattering[33] can make the dominant contribution to the signal. For runaway electrons, the pitch-angle scattering rate is modified by synchrotron losses;[34] also, the conventional Coulomb scattering rate is modified for collisions with impurities that retain bound electrons.[35] For fast ions, charge-exchange reactions[5,36] with injected or edge neutrals can play an important role in evolution of the distribution function.

C. Microscopic motion and macroscopic transport

Not all waves cause macroscopic transport. Consider a small amplitude, oscillating azimuthal electric field E_θ in a solenoid with uniform axial magnetic field $\mathbf{B} = B_0\hat{z}$. The electric field causes radial $\mathbf{E} \times \mathbf{B}$ drifts of the particles. However, if the wave amplitude gradually increases to a maximum then gradually decreases, after the perturbation has past, the particles will all return to their initial position. No radial transport has occurred.

Our EPs are nearly collisionless. This implies that, on a short timescale, their motion is completely reversible. One could watch a video of the motion over a few wave periods without being able to discern if the video was running forward in time or in reverse.

In contrast, imagine watching a video of a group of similar particles on a longer timescale. Now one could easily tell the direction of time: if the particles spread radially as the video advances, time is in the forward direction. If the particles begin at different positions and cluster together at nearly identical positions, the video has run in reverse. Irreversible motion appears when one considers groups of particles on an intermediate timescale. In this context, "intermediate" means longer than several wave periods but shorter than the collisional timescale on which the entire distribution function evolves. If δt is the timescale of the reversible motion, Δt is the intermediate timescale, and t is time in a Fokker–Planck equation, our ordering is $\delta t \ll \Delta t \ll t$ (Fig. 8). The statistics of the microscopic kicks determines the type of macroscopic transport that occurs on the intermediate timescale. Similarly, the statistics of intermediate-timescale transport determines the evolution of the distribution function on the long collisional timescale.

To achieve irreversibility, something is needed to disrupt the reversibility of the microscopic motion. There are several possibilities. One possibility is multiple uncorrelated perturbations, such as those that occur when there is a turbulent spectrum of waves. Another possibility occurs in deterministic chaos (Sec. II C). A third possibility is the almost negligible collisions we usually neglect.

Without specifying its precise origin, assume that a mechanism exists that randomizes the effect of the microscopic (reversible) perturbations. Under these circumstances, a relationship exists between the microscopic kicks given to the particles and the consequent transport. A famous example is the random walk of a drunk. The drunk takes steps of uniform length to the right or left $\delta x = \pm \ell$ with equal probability every δt second. A collection of drunks beginning at the same bar will spread out irreversibly in time. As time advances, owing to the equal probability of left/right steps, the average position of the drunks will remain at the origin (the bar) but their distribution will spread according to

$$\langle (\Delta x)^2 \rangle = 2D\Delta t, \tag{9}$$

where the diffusion coefficient D is related to the microscopic motion by

$$D = \frac{(\delta x)^2}{2\delta t}. \tag{10}$$

Here, brackets $\langle \ldots \rangle$ represent an average over the distribution of particles. Equation (9) describes diffusive spreading. The mean square displacement increases with time as t^γ, where $\gamma = 1$.

More realistic distributions of microscopic kicks can also produce diffusive behavior. Assume a normal distribution of kicks with probability

$$p(x)dx = \frac{1}{\sqrt{2\pi}\delta x} \exp \frac{-0.5x^2}{(\delta x)^2} \tag{11}$$

that occur every δt seconds. A collection of particles that begin at the origin will expand diffusively with the same equations as for the drunken random walk.

Different distributions of microscopic kicks produce different macroscopic spreading. In general, the relationship between the microscopic probabilities and the macroscopic behavior is governed by a "master" equation that relates the probability that the system is found in a given state to the transition (microscopic kick) probabilities.[37] Several simple limits exist, however. If the microscopic kicks are all of comparable magnitude in the same direction, the mean position of the macroscopic distribution grows as $\langle \Delta x \rangle = (\delta x/\delta t)t$. Motion of this type is called "convective." Examples of convective transport for EPs appear in Sec. IV. If the kicks have a distribution of sizes but a preferred direction, a combination of convective and diffusive transport can occur.

Even in the absence of convection, the spreading need not be diffusive. A well-known example is the distribution of kick sizes adopted by many foraging animals. They often take many small steps while feeding at a particular plant, and then take a long step to a different part of the landscape. These produce a distribution of microscopic steps that is a type of "Lévy flight" distribution. The resulting spreading deviates from diffusive scaling [Eq. (9)]; instead, the population spreads as t^γ with $\gamma > 1$. When $\gamma > 1$, the spreading is called "super-diffusive." When $\gamma < 1$, the spreading is called "sub-diffusive." Sub-diffusive transport occurs when large-amplitude kicks are rarer than in the normal distribution of Eq. (11). Figure 9 illustrates the relationship between microscopic kick probabilities and macroscopic transport for several simple cases that are relevant for EP transport.

Sub-diffusive, diffusive, and super-diffusive spreading are all observed for EPs and analyzed theoretically.[39] A particularly clear example was measured on the TORPEX toroidal device. Beams of energetic lithium ions with different energies were launched through transient turbulent electrostatic fluctuations called "blobs" and their mean square displacement was measured at various distances from the source (Fig. 10).[38] Simulations explained the different behavior that was observed.[40] On occasion, the blobs imparted a large $\mathbf{E} \times \mathbf{B}$ kick to lower-energy fast ions. The resulting distribution of kicks resembling Lévy flights produced super-diffusive transport with $\gamma > 1$; this is like the case illustrated in Figs. 9(e) and 9(f). In contrast, for higher energies, the increased grad-B drift caused the fast ions to drift vertically through the electrostatic structures so rapidly that the radial displacement was reduced, causing a truncated kick distribution like the one illustrated in Fig. 9(g); the resulting macroscopic transport was sub-diffusive [Fig. 9(h)].

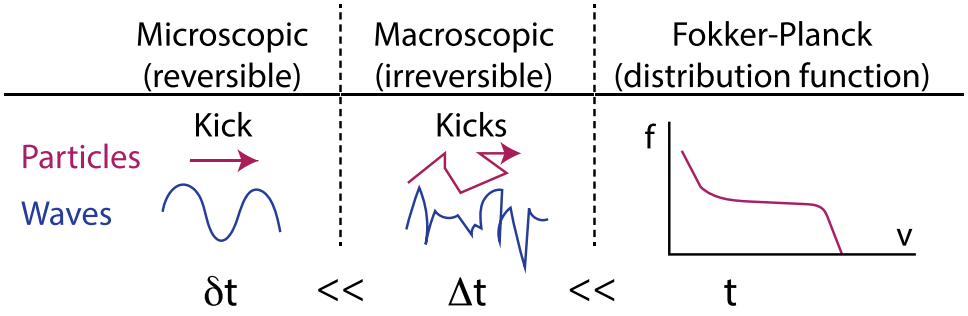

FIG. 8. Illustration of the different timescales governing EP transport. The δt timescale is limited to a few wave periods; the kick received by the particle is deterministic and reversible. The Δt timescale involves many wave periods and multiple kicks; irreversibility of a population of particles appears on this time scale. On the t timescale, the entire distribution function evolves due to the combined action of irreversible transport, collisions, and processes that create and destroy EPs.

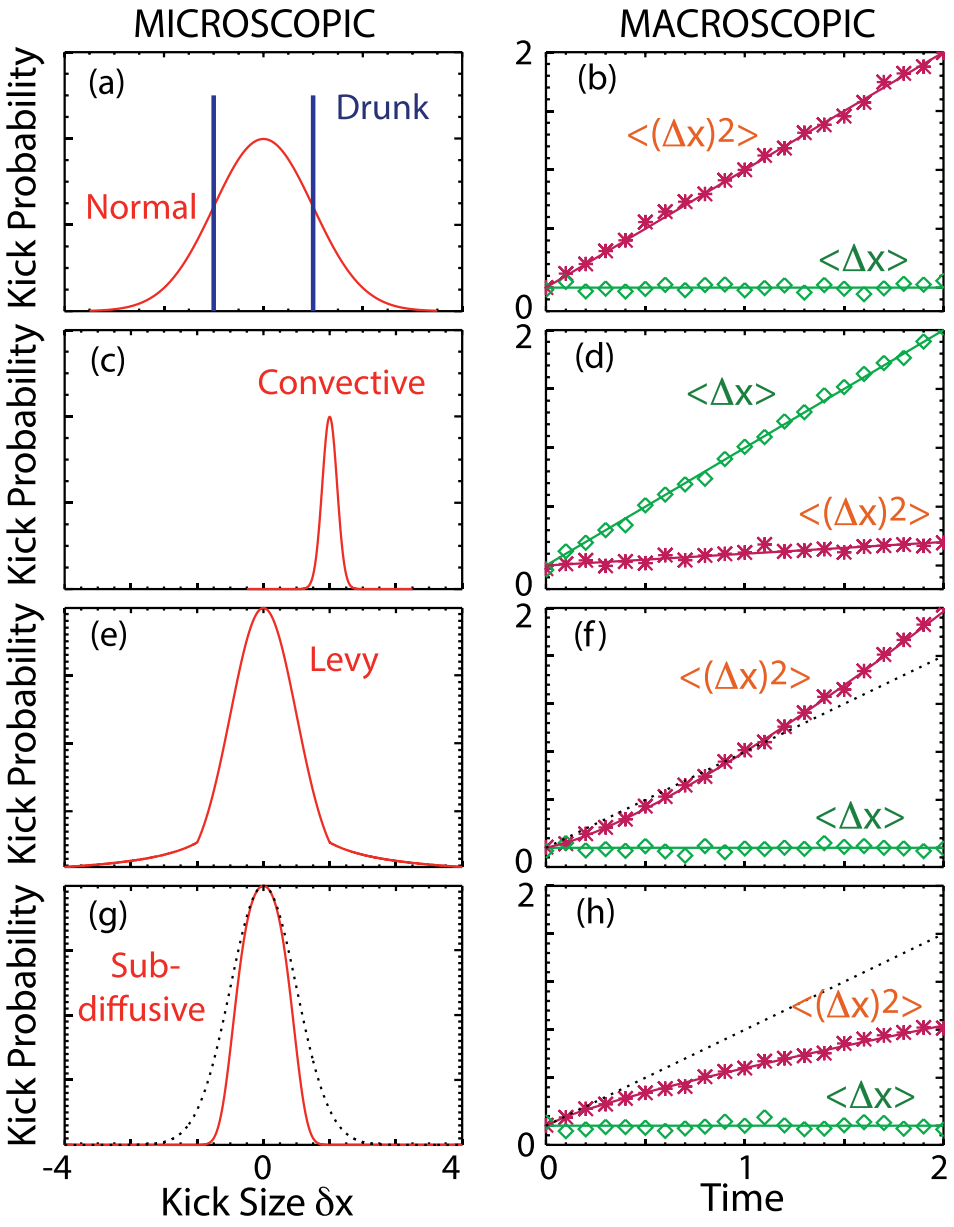

FIG. 9. Sketches illustrating the relationship between (left column) microscopic kicks δx and (right column) the resulting macroscopic transport Δx. (a) Drunk random walk probabilities (thick bars) and a Gaussian distribution (line) produce (b) diffusive spreading $\langle(\Delta x)^2\rangle$ that increases linearly with time but the mean position $\langle\Delta x\rangle$ is zero. (c) When the kicks have a preferred direction (d) convective transport occurs: The mean position $\langle\Delta x\rangle$ increases linearly with time. (e) The Lévy flights of foraging animals and transport by plasma "blobs" produce (f) super-diffusive transport that spreads faster than t^1. (g) If large kicks are suppressed (h) sub-diffusive transport that spreads more slowly than t^1 occurs. Dotted lines in panels e-f represent diffusive behavior.

The concept of random, irreversible kicks is widely employed in theories of EP transport. For example, in cyclotron heating, owing to the resonant interaction described in Sec. IV, particles receive a kick in energy when their orbits traverse locations where $\omega = \omega_c$, causing diffusion in velocity space.[2] Random kicks are readily incorporated into codes that use Monte Carlo markers to represent energetic particles. For example, randomly applied kicks in different portions of phase space successfully model EP interactions with Alfvén waves.[41]

IV. RESONANCE

This section begins by explaining the fundamental conditions for wave-particle resonance, Eq. (13). Next (Sec. IV B), the relationship between the amplitude of the perturbing field and the width of the resonance is explained. Section IV C explains why collisionless wave-particle trapping becomes irreversible. The relationship between wave-particle trapping and mode stability is briefly discussed in Sec. IV D. Section IV E describes the emergence of chaotic orbits caused by particle trapping in wave-particle resonances. Finally, Sec. IV F summarizes the main points of this section.

A. Conditions for resonance

Whether a particle is resonant or non-resonant depends upon the phase Θ between the particle and the wave. Consider the simple case of an ion gyrating in a uniform magnetic field in the presence of an electric field of frequency ω that is spatially uniform and linearly

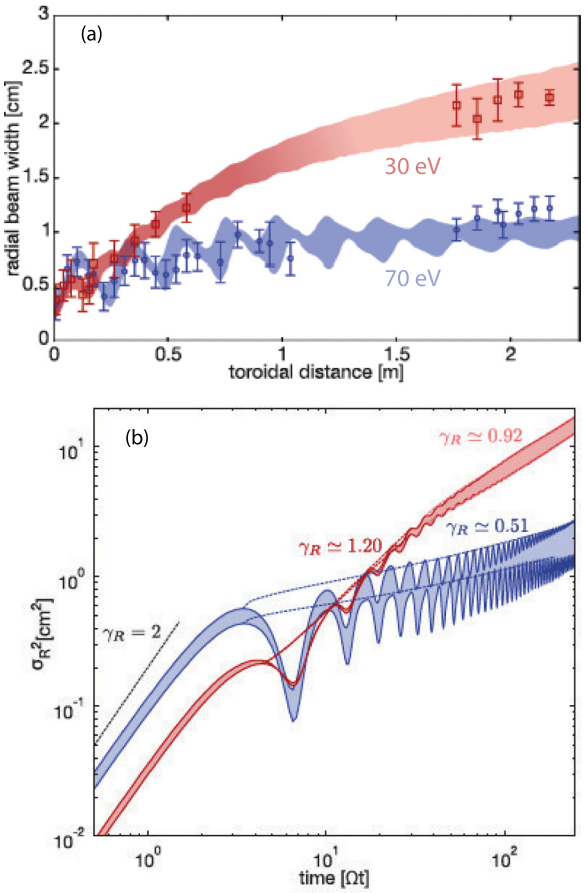

FIG. 10. (a) Measurements (symbols) and simulations (shaded curves) of the spreading of a super-thermal lithium beam in the small toroidal device TORPEX in the presence of transient electrostatic turbulent "blobs." The electron temperature is a few eV and the ions are even colder, so both the 30 eV and 70 eV ions are super-thermal. The visible reversible oscillations of the beam width are caused by the gyromotion. Since the velocity and pitch of the EPs are approximately constant, the toroidal distance is proportional to time. (b) Inferred scaling of the beam spreading σ_R vs time. Owing to the initial velocity spread of the beam, the initial spreading is ballistic, i.e., $\langle(\Delta x)^2\rangle \propto t^2$. For ions of 30 eV, the transport is then super-diffusive with a transport exponent $\gamma \simeq 1.2$ during approximately four gyromotions and finally close to a diffusive process, $\gamma \simeq 1$. For ions of 70 eV, the transport is sub-diffusive with $\gamma \simeq 0.51$. Time is normalized to the ion gyroperiod. Reproduced with permission from Bovet *et al.*, Phys. Rev. E **91**, 041101(R) (2015).[38] Copyright 2015 American Physical Society.

polarized. If the wave frequency matches the cyclotron frequency, the ion always sees an electric field that points in the direction of its horizontal motion [Fig. 11(a)]. The ion is continuously accelerated and its perpendicular energy steadily increases [Fig. 11(e)]; consequently, the first adiabatic invariant $\mu = W_\perp/B$ is not conserved. The perturbation has violated the second criterion for conservation of an adiabatic invariant (Sec. III A).

Note that whether the ion gains or loses energy depends upon its initial phase with respect to the wave. If the initial phase is flipped 180°, the ion continuously loses energy rather than gains energy. Nevertheless, $W_\perp$ has changed and μ is not conserved.

Now consider a wave where $\omega \neq \omega_c$. Now the ion gains energy for a while but subsequently loses any gained energy when the ion sees **E** of opposite phase [Fig. 11(d)]. If the electric field is sufficiently small, the time-averaged change in $W_\perp$ is zero and the time-averaged magnetic moment μ is conserved.

Note that, for resonance to occur, the electric field need not accelerate the ion on the entire orbit. Imagine that the electric field of Fig. 11(a) only existed in the upper half of the orbit. If $\omega = \omega_c$, the ion would still gain energy on every orbit; if $\omega \neq \omega_c$, the ion would still gain energy for a few cycles, and then lose an equal amount of energy on subsequent cycles. One can imagine an even more complicated spatial structure, where the ion gains energy on 2/3 of the orbit but loses energy on 1/3. If $\omega = \omega_c$, $W_\perp$ would still change every cycle and μ would not be conserved.

The instantaneous power a particle of charge q gains from the wave is $dW/dt = q\mathbf{E}\cdot\mathbf{v}$. The energy gained in an orbit is $\Delta W = \oint(dW/dt)dt$ or

$$\Delta W = \oint q\mathbf{E}\cdot\mathbf{v}\,dt = q\oint \mathbf{E}\cdot d\mathbf{l}, \tag{12}$$

where the integral is over the orbit. Evidently, as long as $\oint \mathbf{E}\cdot d\mathbf{l}$ is nonzero, a resonant ion exchanges energy with the wave.

It is not essential that the ion completes its orbit in a single cycle of the wave; the wave can oscillate multiple times in a cyclotron period and still exchange an increment of energy every orbital period. This occurs, for example, in high harmonic cyclotron heating, where finite values of $k_\perp\rho_c$ yield non-zero values of $\oint \mathbf{E}\cdot d\mathbf{l}$ after a cyclotron orbit. ($k_\perp$ is the perpendicular component of the wavevector.) As long as ΔW is non-zero and remains the same every orbital period, resonance still occurs. In other words, the resonance condition is $\omega = l\omega_c$, where l is an integer.

Although we have only considered the gyromotion, all of these principles are readily generalized to include other aspects of the orbital motion. Considering orbits with the three periodicities ω_c, ω_ϕ, and ω_θ, the generalized resonance condition is

$$\omega = l\omega_c + m\omega_\theta + n\omega_\phi, \tag{13}$$

where l, m, and n are integers. Equation (13) states that resonance occurs when the phase of the perturbation changes by a multiple of 2π after the particle has completed a cycle of its periodic motion.

The orbital frequencies in Eq. (13) are averaged over the relevant orbital motion. For example, in a tokamak, the cyclotron frequency ω_c is a function of major radius and therefore varies along the drift orbit; when considering a resonance involving the poloidal orbit, ω_c in Eq. (13) represents the orbit-averaged cyclotron frequency.

In practice, it is often the case that one or more of the integers in Eq. (13) is zero. For example, if the cyclotron frequency ω_c is much larger than the other orbital frequencies, the resonant interaction can take place locally on a portion of the orbit. This occurs in cyclotron heating, where the particles receive a velocity kick in a localized "resonance layer." In this case, the effect of the drift-orbit motion is to introduce a Doppler shift into the local cyclotron resonance condition,

$$\omega - \mathbf{k}\cdot\mathbf{v}_{GC} = l\omega_c, \tag{14}$$

where $\mathbf{k}$ is the wavenumber of the perturbation and $\mathbf{v}_{GC}$ is the guiding-center velocity consisting of $v_\parallel$ and $\mathbf{v}_d$.

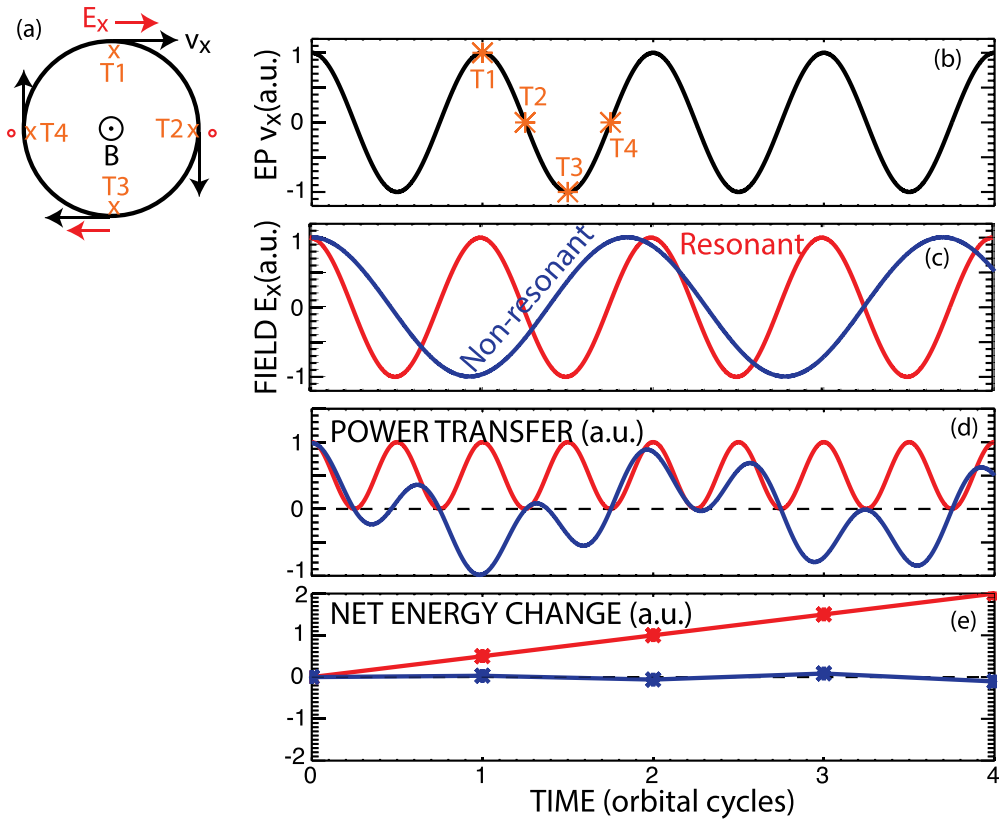

FIG. 11. (a) A gyrating ion in resonance with a linearly polarized electric field with the same frequency as the ion cyclotron frequency. Four times on the orbit are marked. Time evolution of (b) horizontal velocity v_x, (c) horizontal electric field at the particle location E_x, (d) instantaneous power transfer $\mathbf{F}\cdot\mathbf{v}$, and (e) net energy change $\int \mathbf{F}\cdot\mathbf{v}\,dt$ for a resonant wave with $\omega=\omega_c$ (red) and a non-resonant wave with $\omega=\omega_c/1.7$ (blue).

When the frequency of the perturbation is small compared to the cyclotron frequency, μ is conserved and the cyclotron term in the resonance condition [Eq. (13)] is omitted, $\omega = m\omega_\theta + n\omega_\phi$. Naively, for a perturbation with toroidal mode number n' and poloidal mode number m', one might expect that the strongest resonance (i.e., the one with the largest value of $\oint \mathbf{E}\cdot d\mathbf{l}$) would occur for $n=n'$ and $m=m'$ but, because of the large EP orbits, that is not generally the case. To take this effect into account, some authors define a "kinetic resonance"[42] or perform "orbit-based resonance analysis"[43] that explicitly distinguishes the helicity of the strongest resonance from the helicity of the perturbing mode. In an axisymmetric device, resonance does require that $n=n'$ but energy exchange can be appreciable for multiple values of m. For example, for passing particles in a toroidal device, the orbit shift due to drift is primarily $m=1$, a shift outward of a co-moving particle and a shift inward of a counter-moving particle. This shift coupled with the m' value of the perturbation often leads to strong resonances at $m=m'\pm1$. In a stellarator, appreciable energy change can also occur for $n=n'+\nu N$,[44] where ν is an integer and N is the number of periods of the helically symmetric stellarator coils. In general, multiple values of l, m, and n can contribute important resonances.

Examples of multiple important resonances for a low-frequency tokamak perturbation appear in Fig. 12. The orbital frequencies ω_ϕ and ω_θ are functions of the constants of motion, so orbits that satisfy the resonance condition appear in different parts of phase space. For the examples of Fig. 12, $l=0$ and n is equal to the toroidal mode number of the Alfvén wave n', so the multiple resonances occur at harmonics of the poloidal bounce frequency ω_θ.

It is instructive to examine why the example shown in Fig. 12(b) has so many important resonances. Numerous thermal-particle orbits could satisfy Eq. (13) for different values of l, m, and n but relatively few of these would exchange appreciable energy with the wave. The complexity of EP orbits accounts for the difference. The example of Fig. 12 is for a tokamak condition with EP orbits that deviate far from flux surfaces. For this condition, the energy-exchange term depends upon $\oint \mathbf{E}\cdot\mathbf{v}_d$, where $\mathbf{v}_d$ is the drift velocity.[47] Imagine rewriting the integral in terms of an integral over the poloidal angle θ; to do so, one would decompose $\mathbf{v}_d$ in terms of a Fourier series,

$$v_d = \sum_m A_m e^{im\theta},$$

where the A_m are Fourier coefficients. For a thermal particle, only a few coefficients are appreciable but many Fourier coefficients are required to describe a complex EP orbit. It is this orbital complexity that makes the energy exchange large for many values of m in Fig. 12(b).

In practice, evaluation of the resonance condition [Eq. (13)] is readily performed, as only the equilibrium orbits and mode frequency are needed for the calculation. However, to tell if a resonance is *important*, one needs detailed measurements or modeling of the perturbation in order to evaluate $\oint \mathbf{E} \cdot d\mathbf{l}$ for each resonance. Figure 12(a) is an example of the simpler evaluation, while Fig. 12(b) is an example of a calculation of actual energy exchange.

Our discussion to this point has emphasized the energy exchange $\oint \mathbf{E} \cdot d\mathbf{l}$. However, the resonance condition [Eq. (13)] applies even for a static magnetic perturbation with $\omega = 0$ and $\mathbf{E} = 0$. Since $\mathbf{F} \cdot \mathbf{v} = q(\mathbf{v} \times \mathbf{B}) \cdot \mathbf{v}$ is identically zero for static magnetic fields, they never alter the EP *energy*; nevertheless, resonance with a static magnetic field can alter the EP *momentum*, causing a constant-of-motion to change. In this case, rather than the energy exchange considered in the derivation of Eq. (12), one considers the impulse delivered by the perturbation each cycle,

$$\Delta \mathbf{P} = \oint \mathbf{F}\, dt = q \oint \mathbf{v} \times \mathbf{B}\, dt, \tag{15}$$

where $\Delta \mathbf{P}$ is the corresponding change in momentum. As with energy exchange, for a non-resonant EP orbit, the particle receives random small kicks each cycle; these kicks average to zero without altering a constant-of-motion. On the other hand, for a resonant EP orbit, the momentum kicks add secularly and a constant-of-motion is broken. When a static perturbation and EP orbit satisfy $0 = m\omega_\theta + n\omega_\phi$ [a special case of Eq. (13)], momentum-altering resonance can occur. An example of breaking of the toroidal canonical angular momentum P_ϕ through resonant interaction with a static magnetic field perturbation appears in Sec. VIII.

A simple demonstration of cyclotron resonance was performed for EPs in a long solenoidal machine, the Large Plasma Device (LAPD). Alfvén waves that produced azimuthal electric fields were launched at one end of the device and a beam of lithium ions on helical orbits orbited through the wave field. When the Doppler shifted wave frequency $\omega - k_\parallel v_\parallel$ matched the EP cyclotron frequency ω_c, large spreading of the beam was observed. A secondary peak with reduced spreading was also observed when $\oint \mathbf{E} \cdot d\mathbf{l}$ accelerated the ions in one direction for 2/3 of a cycle and in the opposite direction for 1/3 of the cycle.[48,49]

B. Resonance width

In general, the orbital frequencies ω_c, ω_θ, and ω_ϕ are complicated functions of phase-space coordinates so the resonance condition [Eq. (13)] is only satisfied on a narrow curve in phase space, as in Fig. 12(a). In reality, however, resonances are broadened to span a region in phase space. [This broadening is apparent in Fig. 12(b).] Particles with a slight mismatch between their orbital frequencies and the wave frequency get trapped in the wave, as in nonlinear Landau damping. This section examines the relationship between the resonance width and mode amplitude, showing that the broadening of the resonance is typically proportional to the square root of the perturbation amplitude [Eq. (19)].

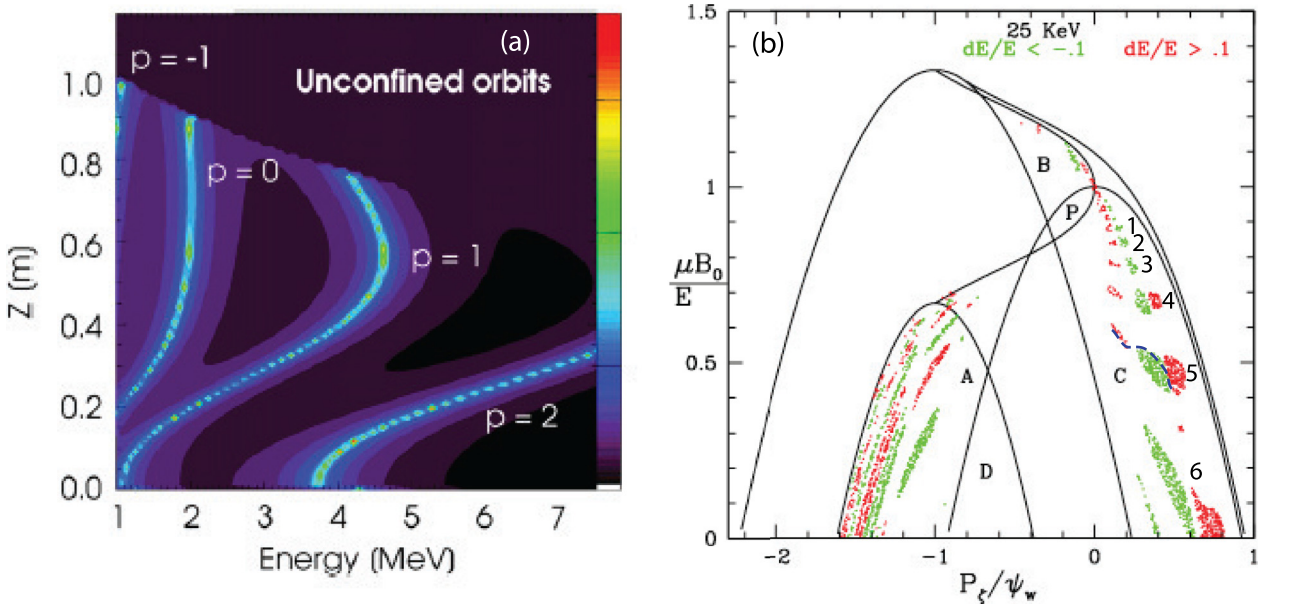

FIG. 12. Examples of resonance calculations. (a) Multiple resonances in the JET tokamak. High energy protons accelerated by ion cyclotron heating resonate with an $n = 3$ Alfvén eigenmode. The plotted trapped particles have their turning points at the major radius where the RF wave resonates with ω_c, so the elevation of the turning point and the particle energy suffice to enumerate the orbits. The curves indicate different possible resonances that satisfy $\omega = p\omega_\theta$. Reproduced with permission from Pinches *et al.*, Nucl. Fusion **46**, S904 (2006).[45] Copyright 2006 International Atomic Energy Agency. (b) Calculated energy exchange of 25 keV deuterium beam ions with a 90 kHz, $n = 2$, $m' = 9$ Alfvénic perturbation in the DIII-D tokamak. Each resonance has adjacent regions of energy loss and gain; each red/green pair is caused by a different resonance. The numbers beside many of the pairs indicate the value of m in the $\omega = n\omega_\phi + m\omega_\theta$ resonance condition. The dashed line indicates where the $m = 5$ resonance is satisfied exactly. The solid lines demarcate different topological regions. The ordinate is the normalized magnetic moment and the abscissa is the normalized toroidal canonical angular momentum. Adapted with permission from White *et al.*, Plasma Phys. Controlled Fusion **52**, 045012 (2010).[46] Copyright 2010 Institute of Physics Publishing.

As a simple example, consider the resonance of an EP with a low-frequency wave in a tokamak. Because μ is conserved, the equilibrium orbit is governed by the guiding center Hamiltonian of Eq. (6). A simple helical wave-particle resonance of form $H_I = -V\cos(n\phi - m\theta - \omega t)$ perturbs the Hamiltonian. Here, V is a constant. From $dW/dt = \partial H/\partial t$ and $dP_\phi/dt = -\partial H/\partial\phi$, we find that $ndW/dt + \omega dP_\phi/dt = 0$, so

$$nW + \omega P_\phi = constant. \tag{16}$$

Consequently, a perturbation consisting of a single toroidal mode number and frequency can only change P_ϕ and W along a line in the (W, P_ϕ) plane; the changes in the two variables are not independent.

Equation (16) can also be obtained from a quantum-mechanical perspective. The wave and particle exchange both energy and momentum. The exchanged energy is $\Delta W = \hbar\omega$ and the exchanged momentum is $\Delta P_\phi = r\hbar k_\phi$. Since the toroidal wavenumber is $k_\phi = n/r$, it follows that $\omega\Delta P_\phi = n\Delta W$.

To find the nature of these changes, we examine a Poincare section (Sec. II C) produced by this Hamiltonian. To produce the Poincare points, set $n\phi - \omega t = 2\pi k$ and record the values of P_ϕ and $m\theta$ each time $n\phi - \omega t$ advances by 2π. Replace $v_\parallel^2$ in the equilibrium Hamiltonian by the expression for P_ϕ in Eq. (8), and then expand the Hamiltonian around the value of P_ϕ for which the resonance holds, P_0.[50] The Hamiltonian is approximately

$$H \simeq \frac{c}{2}(P_\phi - P_0)^2 - V\cos(m\theta), \tag{17}$$

where c is a constant. Let $Q = m\theta$, a convenient spatial coordinate. To find the Poincare surfaces, set H equal to a constant, $C = -V\cos(Q_0)$, giving

$$\frac{c}{2}(P_\phi - P_0)^2 = V[\cos(Q) - \cos(Q_0)]. \tag{18}$$

Figure 13 shows the resulting Poincare surfaces of particle trajectories in the plane of P_ϕ and $Q = m\theta$, where we take $P_0 = 0$ for simplicity. Note that the Hamiltonian is time dependent, so W is not conserved and, in fact, through Eq. (16), the trajectories in the energy variable have the same form as those in P_ϕ.

Expanding near $Q = 0$, we have $\frac{c}{2}P_\phi^2 = V(1 - Q^2/2 - \cos(Q_0))$. This is the equation for an ellipse so the O-point at $Q_0 = 0$ is an elliptic point. Expanding about $Q = \pi$ with $dQ = \pi - Q$, we find $\frac{c}{2}P_\phi^2 = V[-1 + Q^2/2 - \cos(Q_0)]$, an equation for a hyperbola. This hyperbolic point, an X-point, is at $\cos(Q_0) = -1$. The "separatrix" that separates particles that are trapped by the finite-amplitude wave from those that are not is given by curves that pass through the X-points. The region within the separatrix in Fig. 13 is called an island. In terms of P_ϕ, the full width of the island is

$$\delta P_\phi = 4\sqrt{V/c}. \tag{19}$$

All particles within the separatrix are trapped in the resonance and circulate around the elliptic point. As they do this, both the energy and the canonical momentum P_ϕ change periodically. Particles outside the separatrix are not resonant, but they still experience changes of P_ϕ and W that are periodic and adiabatic.

For this Hamiltonian, an EP whose motion in θ and ϕ is related by the ratio n/m satisfies the resonance condition, Eq. (13). Particles that satisfy the resonance condition exactly are at the elliptic or hyperbolic point of the resonance.

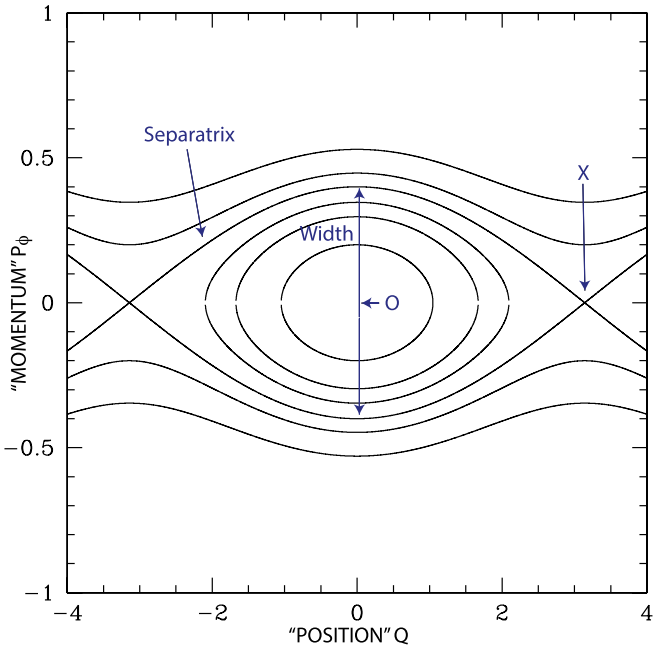

FIG. 13. Poincare surfaces of a resonance in an axisymmetric device produced by a low-frequency mode that depends upon $n\phi - m\theta - \omega t$. The elliptic "O-point" and hyperbolic "X-point" that are the exact solutions of the resonance condition are marked. Particles are trapped within the separatrix that passes through the X-point. The width of the resonance is marked.

C. Irreversibility for particles trapped in a resonance

The motion of particles that are trapped in a wave-particle resonance becomes ergodic.[51] Eventually, on average, all particles trapped by the wave adopt the constants-of-motion of the exact resonance. This section explores the origin of irreversibility for the example of Fig. 13.

To find the rate of rotation about the O-point, differentiate Eq. (17) with respect to time, giving

$$c(P_\phi - P_0)\dot{P}_\phi = V\sin(Q)\dot{Q}. \tag{20}$$

However, $\dot{P}_\phi = -\partial_\phi H = nV\sin(Q)$, giving

$$\dot{Q} \simeq n\sqrt{V/c}\sqrt{\cos(Q) - \cos(Q_0)}, \tag{21}$$

with Q_0 the initial point of the trajectory. The time to complete an orbit around the elliptic point is $T = 4\int_0^{Q_0} dQ/\dot{Q}$, giving

$$T = \frac{4}{n\sqrt{V/c}}\int_0^{Q_0}\frac{dQ}{\sqrt{\cos(Q) - \cos(Q_0)}}. \tag{22}$$

For small Q_0, this is $T = 4/\left(n\sqrt{2V/c}\right)$, and for $Q_0 = \pi$, the integral diverges. The frequency about the elliptic point is proportional to the island width, or the square root of the perturbation amplitude, and it goes to zero as the separatrix is approached.

In Fig. 14 is shown an actual Poincare plot of a 50 kHz mode resonating with 25 keV particles in a tokamak. The circulation of particles around the hyperbolic point is shown at the right, with snapshots at increasing time intervals. The rotation is most rapid near the elliptic point, and goes to zero at the separatrix. Because of the variation of the rotation rate with the distance from the elliptic point, with increasing time, the mixing of different energies and values of P_ϕ occurs at smaller and smaller distances, until it finally reaches interparticle scales. At this point, even an infinitesimal collision rate is sufficient to guarantee irreversibility and the average value of energy and P_ϕ of the entire trapped population is the same as that of the elliptic point.

D. Relationship between particle trapping, mode growth, and mode amplitude

Equation (19) states that the resonance width in phase space is proportional to the square root of the perturbation amplitude. From the perspective adopted in the majority of this review, the perturbation amplitude is an independent parameter that will determine the consequent EP transport. It could be experimentally measured. It could be externally controlled by coils or antennas. It could be the result of an instability whose amplitude is governed by interaction with the thermal plasma, such as an MHD instability. Or it could be an EP-driven instability. In the latter case, there is an interplay between the wave-particle trapping, the properties of the EP distribution function, and the mode amplitude that is briefly explored here.

As discussed in Sec. IV C, all EPs that are trapped in the resonance eventually adopt the constants-of-motion of the exact resonance. As in Landau damping, whether these nonlinearly trapped particles deliver or extract energy from the wave depends upon the slope of the distribution function f in the vicinity of the resonance. In Landau damping, the relevant slope is $\partial f/\partial v_\parallel$; more generally, the relevant slope is across the resonance in constants-of-motion space and involves terms such as $\partial f/\partial W$ and $\partial f/\partial P_\phi$. If more particles gain energy than lose energy, the wave damps. If the energy gained by the wave exceeds any intrinsic damping, the wave grows.

If there is an imbalance between wave growth and damping, the amplitude of the perturbation changes. There are many possible scenarios for the subsequent evolution of the mode. One possibility is that a balance is achieved between energy extracted from the distribution function and replenishment of the driving gradients; an example of a possible steady-state scenario appears in Ref. 52. If mode growth depletes driving gradients, a burst of transient growth followed by decay can occur. If the flattening of local phase-space gradients causes steepening of neighboring gradients, the mode may chirp in frequency $d\omega/dt$, so that the nonlinear trapping region sweeps through new portions of phase space as the mode evolves. In the Berk-Breizman model (reviewed in Refs. 53 and 54), the relative values of linear drive, mode damping, trapping frequency, and scattering rates determine which of these scenarios occur. A comprehensive discussion of the many possibilities including the role of the mode structure appears in Ref. 55.

E. Orbit stochasticity and island overlap

In the presence of multiple resonances, islands may overlap. When they do, orbits are usually chaotic.

An example appears in Fig. 15(a) for the case of an ion that streams along a magnetic field in the $\hat{z}$ direction in the presence of an electrostatic wave that propagates obliquely to the field. The plot shows where ions with three different initial conditions lie in (z, v_z) space at regular intervals. These three ions satisfy the Doppler-shifted resonance condition [Eq. (14)] $\omega - k_z v_z = \ell\omega_c$ with $\ell = -1, 0, 1$. For the case shown in Fig. 15(a), the amplitude of the wave is small, so the three orbits lie on well-defined curves.

Figure 15(b) shows an example of chaotic orbits that appear when the perturbing electrostatic wave is large. Often some orbits

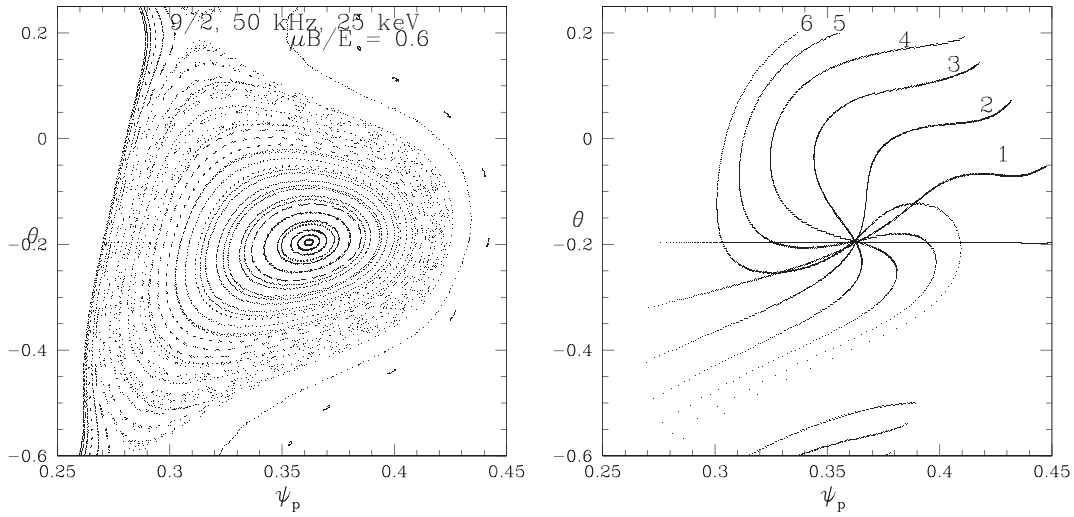

FIG. 14. Circulation of particles within a resonance. At left is shown the Poincare plot given by very many toroidal transits, and at right snapshots taken at fixed time intervals of the particles initially at $\theta = -0.2$, showing the variation of the rotation rate as a function of distance from the O-point.

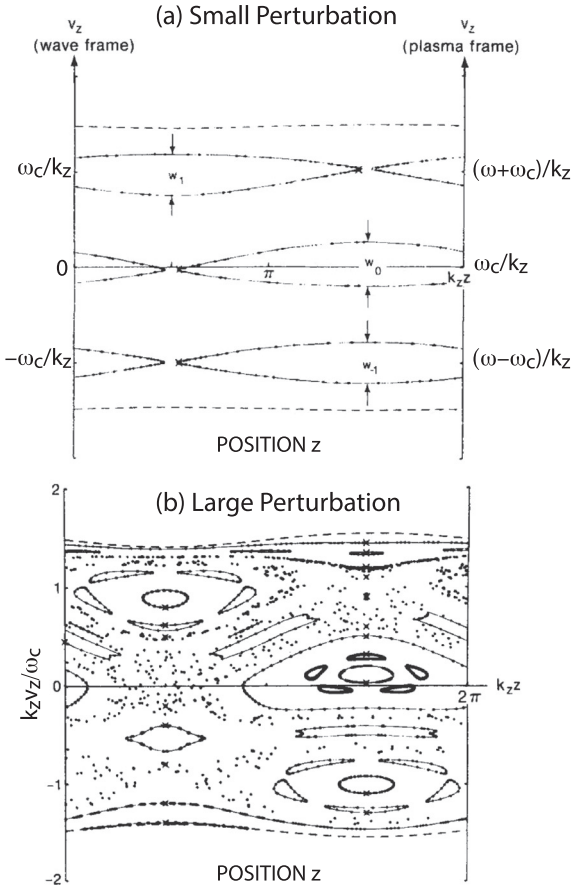

FIG. 15. Poincare plots showing examples of (a) regular and (b) chaotic orbits for an ion in a uniform magnetic field in the presence of a perturbing obliquely propagating electrostatic wave. In the wave frame, resonance occurs when $\omega = l\omega_c$; in the lab frame, resonance occurs when the wave phase velocity ω/k_z matches the parallel particle speed v_z and when $(\omega \pm \omega_c)/k_z = v_z$. The illustrated orbits in (a) are near the separatrices that separate orbits that are trapped in the wave from ones that are not. The wave amplitude is four times larger in (b) than in (a). Adapted with permission from G. R. Smith and A. N. Kaufmann, Phys. Fluids **21**, 2230 (1978).[56] Copyright 1978 AIP Publishing.

remain periodic even when most orbits are chaotic. The solid curves in Fig. 15(b) are examples of regular orbits that persist even when most of phase space is stochastic.

Experts in nonlinear dynamics have extensively analyzed the conditions that result in stochasticity. One helpful concept is the Chirikov or "island overlap" criterion. The labels w_{-1}, w_0, and w_1 in Fig. 15 mark the widths of the three different islands. As discussed in Sec. IV B, the widths grow in size when the amplitude of the perturbation increases. The Chirikov criterion states that when the widths of the islands exceed the distance between islands, stochasticity ensues. Although this criterion is not quantitatively accurate in most situations, it is a useful qualitative guide to ascertain conditions that disrupt confinement.

Stochasticity leads to increased transport, but the nature of the transport varies in different circumstances, including subdiffusive, diffusive, and superdiffusive transport.[39]

F. Summary of resonance conditions and properties

(1) Resonance occurs when the particle and the wave return to the same initial phase after a multiple of an orbital period.
(2) The initial phase determines whether the particle loses or gains energy but has no impact on whether resonance occurs.
(3) The energy exchange is determined by $\oint \mathbf{E} \cdot d\mathbf{l}$ integrated over the orbit. If this quantity is zero, even if the resonance condition [Eq. (13)] is satisfied, there is no energy exchange. Important resonances have non-zero values of $\Delta W = q \oint \mathbf{E} \cdot d\mathbf{l}$ or $\Delta \mathbf{P} = \oint \mathbf{F}\, dt$.
(4) Particles that do not satisfy the resonance condition [Eq. (13)] are weakly affected by the wave.
(5) For a finite amplitude wave, the particle need not match the resonance condition exactly. Nonlinear trapping captures particles that are slightly out of resonance. The width of this resonance-broadened region increases with the square root of the amplitude of the perturbation [Eq. (19)].
(6) Nonlinearly trapped particles ultimately adopt the constants-of-motion of the exactly resonant particles.
(7) When resonances overlap, orbits become chaotic and transport becomes large.

V. ORBIT AVERAGING OFTEN REDUCES TRANSPORT

When EPs are non-resonant, the large EP orbits often reduce transport below the level experienced by thermal particles. This reduction occurs whenever the spatial structure of the perturbations is comparable to or smaller than the orbit size. The mechanism responsible for this reduction is called "phase averaging."

Consider the simple example illustrated in Fig. 16(a). An EP executes a helical orbit in a solenoid filled with plasma. The plasma contains a low-frequency ($\omega \ll \omega_c$) electrostatic wave with very long parallel wavelength ($k_\parallel \simeq 0$), so the situation is essentially two-dimensional. The electrostatic potential fluctuations are described by $\Phi = \Phi_0 \cos k_y y$, where k_y is the vertical wavenumber. The electric field associated with this potential causes horizontal $\mathbf{E} \times \mathbf{B}$ displacement of the EP orbit. If the Larmor radius is much smaller than the spatial structure of the electrostatic wave ($k_y \rho_c \ll 1$), the electric field is upward throughout the entire orbit, so the particle always drifts to the right. However, if the Larmor radius is large, the orbit samples regions of both upward and downward electric field. The particle drifts to the right on some of its orbit and to the left on others. Consequently, the net drift is reduced. Mathematically, $\oint \mathbf{E} \cdot d\mathbf{l} \simeq 2E\Delta y$ for the small gyroradius but $\oint \mathbf{E} \cdot d\mathbf{l} \simeq \int E \cos(k_y y)\, dy < 2E\Delta y$ for the large gyroradius. The usual $\mathbf{E} \times \mathbf{B}$ drift is reduced by phase averaging by a factor of $J_0(k_y \rho_c)$.[57] (J_0 is the Bessel function of the first kind.)

An experiment very similar to the simple example of Fig. 16(a) was conducted in the Large Plasma Device (LAPD).[58] A rectangular obstacle placed in the plasma created a sharp density gradient that generated electrostatic fluctuations on the scale of the thermal ion Larmor radius. A beam of energetic lithium ions of variable gyroradius passed through the fluctuations and the spreading of the beam was measured. As expected, beam spreading decreased monotonically with increasing gyroradius [Fig. 16(b)].

In a related experiment on the LAPD,[59,60] the EP gyroradius was held fixed while the scale length of the electrostatic fluctuations was varied. As expected, beam spreading was smallest for small-scale,

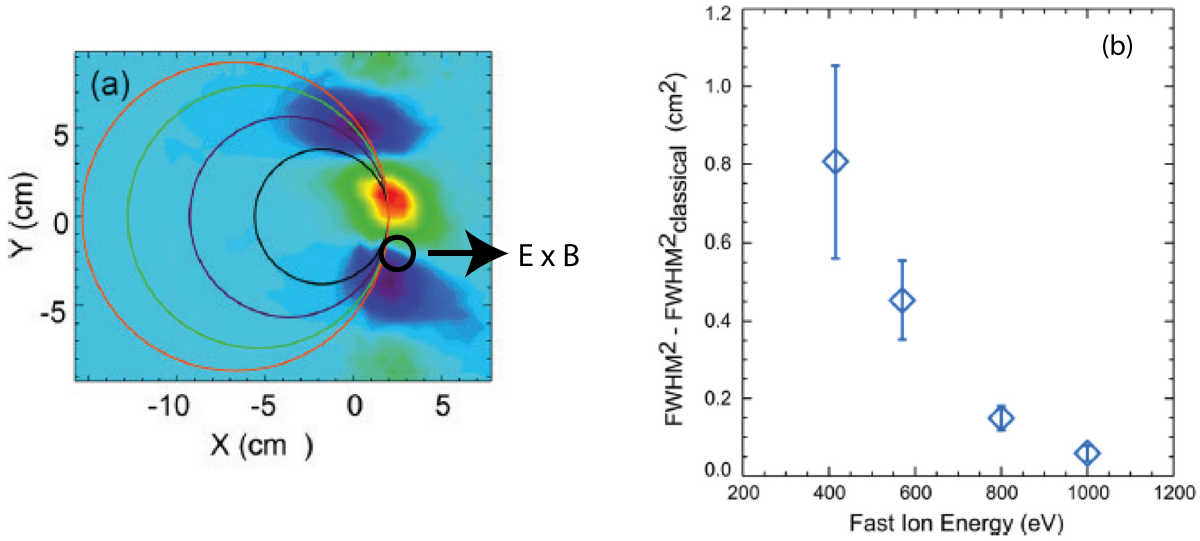

FIG. 16. (a) Phase of fluctuations in ion saturation current measured by a pair of Langmuir probes. The fluctuations were created by a rectangular obstacle placed in the LAPD plasma. The magnetic field is out of the page. The gyroradii of the four measured EP orbits are overlaid. Also overlaid is the gyroradius of a low energy ion that "sees" a constant horizontal $\mathbf{E} \times \mathbf{B}$ drift. (b) Measured spreading of the EP beam caused by the potential fluctuations vs EP energy. The parallel velocity was held constant throughout the scan. The calculated gyro-averaged density fluctuation decreases by a factor of two between 400 and 1000 eV.[58] Adapted with the permission from Zhou *et al.*, Phys. Plasmas **19**, 055904 (2012).[59] Copyright 2012 AIP Publishing.

highly coherent fluctuations where phase averaging is particularly effective. When the scale of the fluctuations was larger or the collection of small-scale fluctuations was more turbulent, the EP transport was increased. A similar example from the TORPEX device was already presented in Fig. 10. Owing to orbit averaging, the highest energy ions suffer far less transport than lower energy EPs.

This is a general result observed in many experiments: when EPs are non-resonant, they generally have much better confinement than thermal particles. As long as the scale length of the perturbation is smaller than characteristic EP orbit sizes, the transport associated with any type of perturbation is reduced.

As an example of reduced transport by electromagnetic perturbations, consider the transport of runaway electrons in a tokamak that contains stochastic fields associated with electromagnetic turbulence. Since electrons travel rapidly along magnetic field lines, wandering field lines contribute to diffusive electron transport. The situation for thermal electrons was analyzed using random-walk arguments in a famous paper by Rechester and Rosenbluth.[61] Assume the field lines diffuse radially by an amount δr each transit L of the torus so, by Eq. (10), $D_f \simeq (\delta r)^2/(2L)$. Rare collisions provide sufficient decorrelation so that an electron takes a step every toroidal transit; hence, $\delta t = L/v_\parallel$. The resulting particle diffusion coefficient D_e is

$$D_e \sim D_f v_\parallel, \tag{23}$$

where $v_\parallel$ is the electron velocity parallel to $\mathbf{B}$. According to Eq. (23), because faster electrons travel farther, the electron diffusion increases with $v_\parallel$. As predicted, the experimentally measured confinement time of low energy runaways (0.4–1.0 MeV) is 10%–30% of the thermal electron confinement time.[62] However, as the energy increases further, another effect becomes important: The curvature drift increases and the orbital deviations become larger than the scale length of the electromagnetic fluctuations.[63] Phase averaging occurs. As a result, after an initial decrease, the electron confinement time for MeV runaway electrons increases with increasing energy, becoming an order of magnitude larger than the thermal electron confinement time for runaways of 8–22 MeV (Refs. 63 and 64) (Fig. 17).

A similar reduction in radial transport by fluctuating electromagnetic fields was observed in the MST reversed field pinch, where, due to orbit averaging, energetic beam ions were much better confined than thermal ions.[65]

The TFTR experiment of Fig. 4 provides yet another example. In that experiment, the rate at which counter-passing fusion products crossed a loss boundary was measured. The diffusion coefficient inferred from the data was $D < 0.1$ m^2/s, much less than typical thermal coefficients of $D \sim 1$ m^2/s.[14]

It can also occur that small perturbations lead to long term complex traps for particles, with the associated Lévy flights producing either subdiffusion or superdiffusion. Subdiffusion is regularly observed in the stochastic field of RFX.[39]

As a final example, consider the transient fields produced in a tokamak when a "sawtooth" internal reconnection event occurs. A sawtooth event generally is initiated by a growing $n = 1$, $m = 1$ internal kink mode that triggers the $n = 0$ "sawtooth crash." (Here, n is the toroidal mode number of the perturbation and m is the poloidal mode number.) Normally, the electron density and temperature profiles flatten at a sawtooth crash, as the scrambled magnetic field lines associated with the reconnection event enable rapid parallel electron transport. This is not necessarily the case for energetic ions, however. In a theory by Kolesnichenko,[66,67] only lower energy ions of a given orbit type experience significant radial transport; due to orbit averaging, higher energy ions are only weakly affected. Additionally, because

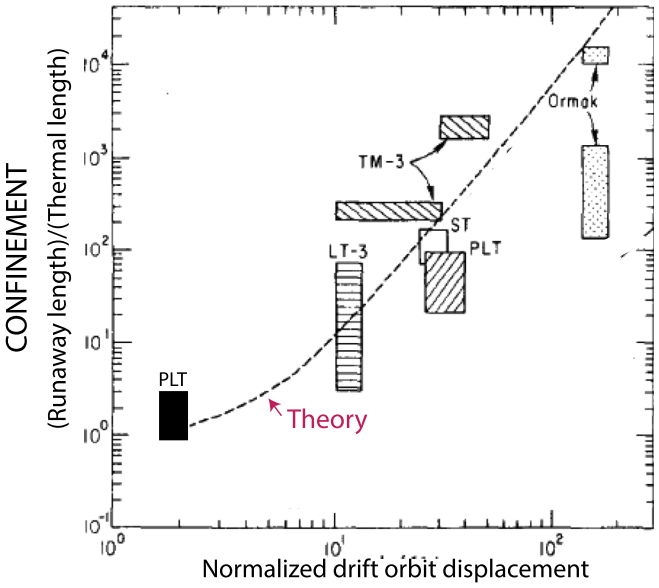

FIG. 17. Improved runaway electron confinement due to drift-orbit averaging in several tokamaks. The ordinate is the ratio of the parallel distance traveled by a runaway before it is lost, normalized to the parallel length traveled by thermal electrons inferred from the thermal electron confinement time. The abscissa is the runaway drift orbit displacement associated with the curvature drift normalized by the assumed scale length of the microturbulence, the thermal ion gyroradius. The curve is a theoretical prediction of the expected dependence. Adapted with permission from H. E. Mynick and J. D. Strachan, Phys. Fluids **24**, 695 (1981).[63] Copyright 1981 AIP Publishing.

their orbit widths are larger, trapped particles of a given energy are less affected than passing particles. The qualitative features of this prediction have been confirmed by many experiments.[68–73]

Although this section has emphasized non-resonant interactions, phase averaging can also reduce the impact of a resonant perturbation. The key requirement for phase averaging is that the orbital size exceeds the scale length of the perturbations, making $\oint \mathbf{E} \cdot d\mathbf{l}$ small.

VI. CONVECTIVE RESONANT TRANSPORT

Under some circumstances, an EP always receives a kick in the same direction, resulting in strong convective transport [Figs. 9(c) and 9(d)]. A famous example of this type of transport is the "fishbone" instability observed in tokamaks. This is a large global mode with an $n = 1$ toroidal structure. The wave produces a poloidal electric field that pushes the particles radially through the $\mathbf{E} \times \mathbf{B}$ drift in the strong toroidal equilibrium magnetic field. For reasons discussed below, the resonant fast ions preserve their wave-particle phase on every wave cycle. After 4–6 kicks outward, the EP is lost [Fig. 18(a)].

Diagnostics that are sensitive to edge losses measure a burst of signal each time the instability rotates past the detector [Fig. 18(b)]. Like a rotating lighthouse searchlight, these periodic bursts pass the observer once each cycle. As expected, the burst has a definite phase with respect to the instability [Fig. 18(b)], namely, the phase where the $\mathbf{E} \times \mathbf{B}$ drift pushes the EP outward. (For the opposite initial phase, an EP is pushed inward, becoming better confined.) In Ref. 75, seven

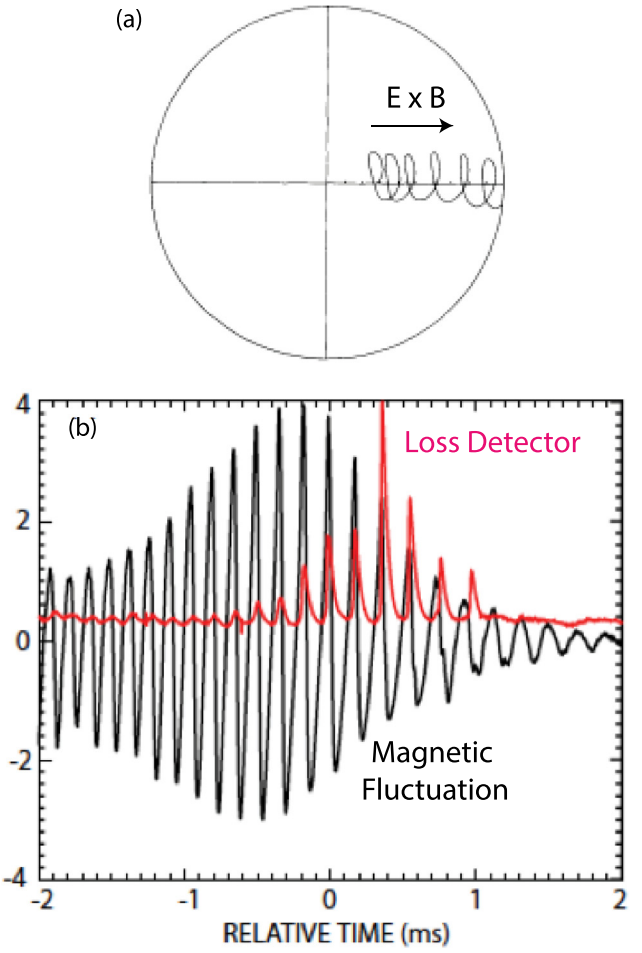

FIG. 18. (a) Projection of a guiding center orbit that experiences convective transport until it is lost to the wall. The calculation is for the "fishbone" instability in the PDX tokamak. Adapted with permission from White *et al.*, Phys. Fluids **26**, 2958 (1983).[74] Copyright 1983 AIP Publishing. (b) Magnetic fluctuation dB/dt and loss-detector signals during an "off-axis fishbone" in the DIII-D tokamak. After a delay, the losses occur with nearly the same phase relative to the mode on every cycle. Reproduced with permission from Heidbrink *et al.*, Plasma Phys. Controlled Fusion **53**, 085028 (2011).[75] Copyright 2011 Institute of Physics Publishing.

different edge diagnostics each measured a definite phase with respect to the mode, depending on their toroidal locations.

The fishbone is a low-frequency mode with a single toroidal mode number n. Because the wave frequency is much lower than the cyclotron frequency, the first adiabatic invariant μ is conserved. Although the energy W and toroidal canonical angular momentum are not conserved, the quantity $nW - \omega P_\phi$ is [Eq. (16)], so the relationship between the energy change in the resonant interaction and the change in P_ϕ is

$$n\Delta W = \omega \Delta P_\phi. \tag{24}$$

Because the toroidal canonical angular momentum contains a dependence on plasma position through its dependence on the poloidal flux [Eq. (3)], Eq. (24) implies a definite relationship between the energy change of the resonant particle and its spatial transport.

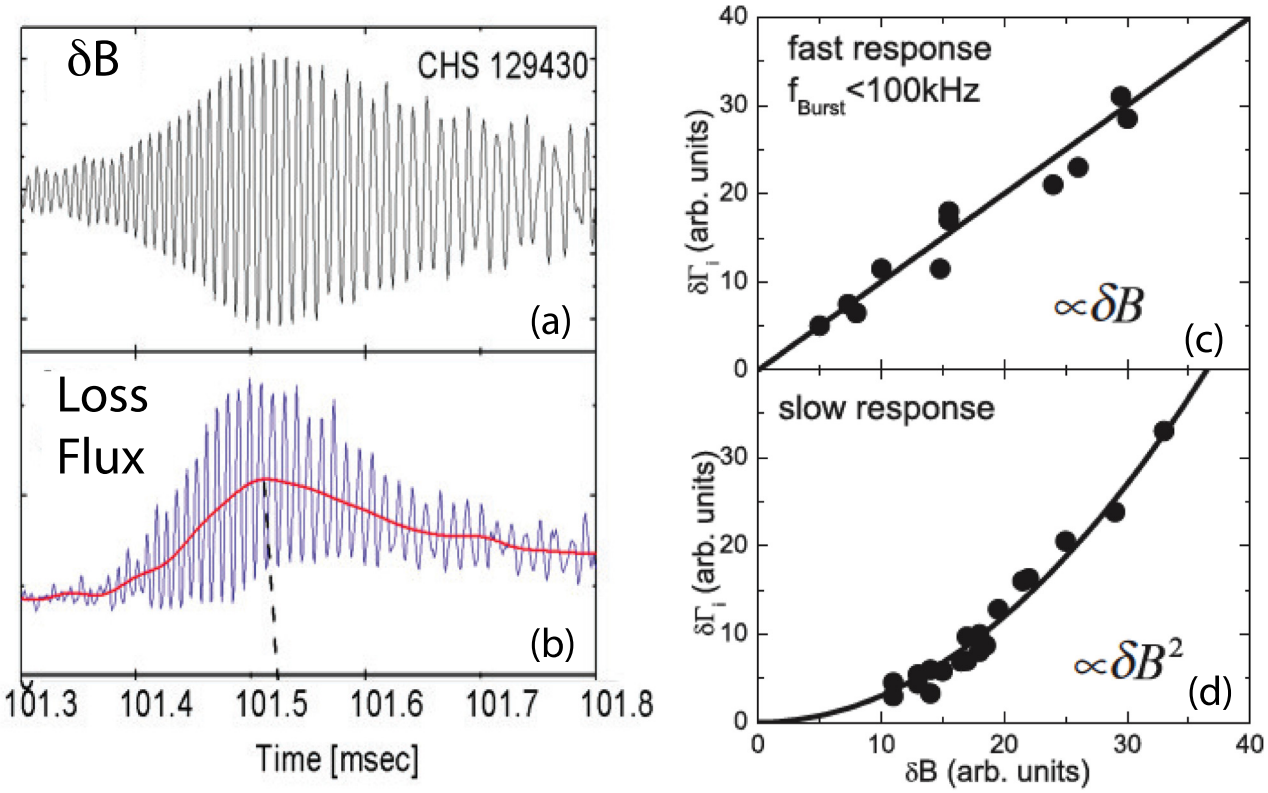

FIG. 19. (a) Magnetic field amplitude δB and (b) fast-ion flux Γ_i at an energetic-particle mode burst on the CHS stellarator. The red line shows the incoherent loss signal. (c) The coherent loss signal scales linearly with the mode amplitude, while (d) the incoherent loss signal scales as δB^2. Adapted with permission from Nagaoka *et al.*, Phys. Rev. Lett. **100**, 065005 (2008).[79] Copyright 2008 American Physical Society.

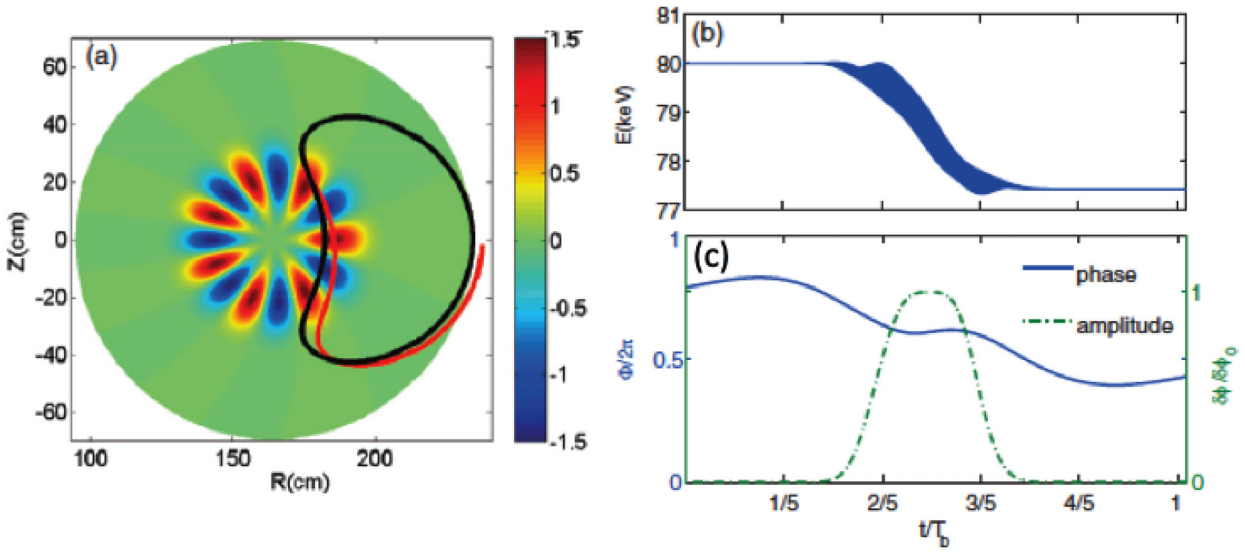

FIG. 20. (a) Projection of a guiding center orbit that passes through an $n = 3$ RSAE on the DIII-D tokamak. The unperturbed trapped-particle orbit (black) is kicked onto a loss orbit (red) by the RSAE; the mode's poloidal phase is indicated by the color bar. (b) Calculated energy loss in the transit through the mode. (c) Mode amplitude (dash-dot line) and wave phase (solid) experienced by the particle. The particle sees nearly constant phase when it traverses the eigenmode. This causes a large radial displacement at the mode frequency. Reproduced with permission from Zhang *et al.*, Nucl. Fusion **55**, 122002 (2015).[81] Copyright 2015 International Atomic Energy Agency.

Equation (24) has important implications for the stability of low-frequency modes that are driven unstable by an EP population. To drive instability, the EPs must impart energy to the wave, so ΔW must be negative for the majority of resonant particles that become trapped by the wave. Under some circumstances, the instability can adapt its frequency to preserve resonance with this clump of resonant particles as they are radially transported. [The wave frequency must change because, in general, ω_c, ω_ϕ, and ω_θ in Eq. (13) are functions of position.] A wave that obeys a dispersion relation associated with an EP population (rather than the dispersion relation of a normal mode of the background plasma) is called an "energetic particle mode" (EPM).[76] Because it preserves the wave-particle phase, an EPM is particularly effective in causing convective resonant transport. A sophisticated discussion of conditions that support an EPM appears in Sec. 4 of Ref. 55.

The predicted reduction in energy is observed experimentally. In the example of Fig. 18(a), the neutral beams were injected at 45 keV but the largest and most coherent loss signal was at ∼35 keV.[77] A change of energy of $\Delta W \simeq -10$ keV is expected for beam ions that transport from the plasma center to the edge in a wave of the observed frequency and mode number.

A common feature of EP losses caused by convective resonant transport is a linear dependence on the mode amplitude. This is readily understood: The $\mathbf{E} \times \mathbf{B}$ drift is linearly proportional to the amplitude of the electric field E. Examples abound. The losses caused by fishbones scaled linearly with mode amplitude.[78] A probe that directly measured the mode amplitude and EP losses was inserted into the CHS stellarator.[79] During an energetic particle mode, the portion of the signal that oscillated at the mode frequency (also called the coherent signal) scaled linearly with the mode amplitude, while the incoherent signal scaled quadratically with mode amplitude (Fig. 19). (The latter dependence is often observed for the diffusive resonant transport discussed in Sec. VII) Similarly, coherent losses measured at the edge of the ASDEX-Upgrade tokamak scaled linearly with the amplitude of a type of Alfvén wave known as a toroidal Alfvén eigenmode (TAE) but the incoherent losses scaled with the square of the mode amplitude.[80]

Under some circumstances, losses caused by convective transport can occur even when an EP does not satisfy the usual resonance condition of Eq. (13). Convective losses of this type were caused by an Alfvén wave called a "reversed shear Alfvén eigenmode" (RSAE) on the DIII-D tokamak.[82] The experiment was designed to detect the EP orbit after it made a single transit through a spatially localized RSAE [Fig. 20(a)]. When the wave-particle phase [Fig. 20(c)] stays nearly constant during the transit through the mode, a large $\mathbf{E} \times \mathbf{B}$ drift occurs. Coherent losses are observed with inferred orbital displacements as large as 10 cm.[82,83] This occurs despite the fact that the resonance condition [Eq. (13)] is *not* satisfied by the measured orbit. Presumably, if the particle remained confined, it would regain the lost energy on subsequent transits through the mode but, because it crosses a loss boundary, the interaction is irreversible. This is an example of a constant-of-motion being broken by a large kick, the third criterion listed in Sec. III A.

VII. DIFFUSIVE AND STIFF RESONANT TRANSPORT

In a finite amplitude wave, the resonance condition is broadened (Sec. IV B). However, if the perturbation is small the broadening is modest, so only a small portion of phase space is affected. As a concrete example, the effect of a single EP resonance with an Alfvén wave of amplitude $\delta B/B = 10^{-4}$ is essentially undetectable with available tokamak diagnostics. To achieve appreciable transport, multiple resonances must interact. From the perspective of Sec. III, the additional resonances provide randomizing elements that promote irreversible transport. Multiple resonances can occur because multiple waves cause different resonances, because large EP orbits produce multiple resonant harmonics with a single wave (as in Fig. 12), or both.

When multiple resonances intersect in phase space, diffusive transport often occurs. The associated losses often scale with the

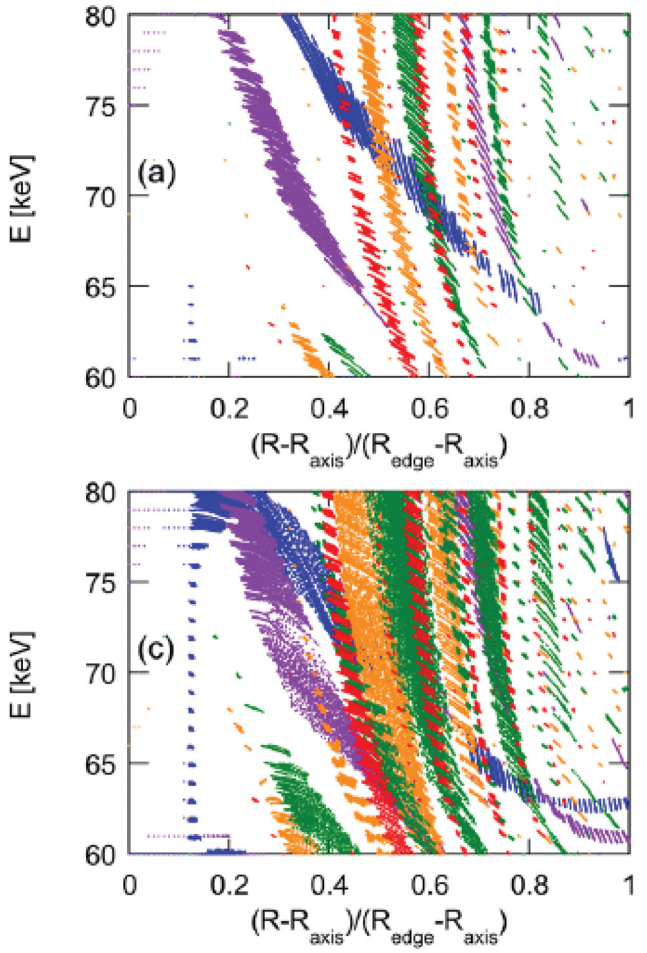

FIG. 21. Simulation results for a DIII-D experiment on the effect of Alfvén eigenmodes on EP transport. Particle trajectories in the phase space of normalized major radius and energy are shown for a typical value of μ for co-passing ions. Only the particles trapped by a wave are plotted. The colors represent Alfvén eigenmodes with different toroidal mode numbers: $n = 1$ (blue), $n = 2$ (purple), $n = 3$ (green), $n = 4$ (orange), and $n = 5$ (red). (a) Condition with weak Alfvén activity. Because the modes are weak, the resonances are narrow. Experimentally, in this condition with few intersecting resonances, EP transport is undetectable. (c) Condition with many unstable Alfvén waves of larger amplitude. The resonances are broader and many intersect. Experimentally, EP transport is strong for these conditions. Reproduced with permission from Todo *et al.*, Nucl. Fusion **56**, 112008 (2016).[85] Copyright 2016 International Atomic Energy Agency.

square of the perturbation amplitude. This amplitude dependence of the transport is readily explained.[84] As previously mentioned, for convective transport or losses of particles besides a loss boundary, linear scaling with amplitude is predicted[84] and observed, as in Fig. 19(a). For multiple resonances, each interaction imparts energy and momentum kicks [Eq. (24)]. If the kicks are random and small amplitude, $\langle(\Delta P_\phi)^2\rangle = 2Dt$ [Eq. (9)], with a diffusion coefficient D that is proportional to the square of the size of the kick [Eq. (10)]. Since the kick sizes are proportional to the wave amplitudes, D scales quadratically with mode amplitude. If, in addition, the transport follows Fick's law ($\Gamma = -D\nabla n$), then the flux Γ is proportional to (amplitude)^2. (Here, ∇n is the EP density gradient in phase space.) Measured incoherent losses with quadratic scaling already appeared in Fig. 19(b). Another excellent example appears in Ref. 80.

Although diffusive transport is one possible response to multiple interacting resonances, another possibility is "stiff" transport. In stiff transport, transport is negligible up to a threshold in mode amplitude, then increases rapidly when the system is driven past the threshold. A condition with stiff resonant transport from multiple small-amplitude waves and multiple resonances per mode has been studied extensively in the DIII-D tokamak. In that experiment, neutral beam ions are the EPs and Alfvén eigenmodes of different types and mode numbers provide the small amplitude perturbing waves. Analysis of the EP orbits using measured mode structures and amplitudes shows the existence of multiple resonances that intersect in phase space (Fig. 21). Below a threshold in the number of modes and their amplitudes, negligible transport is measured but, above this threshold, the phase-space flux of EPs rises rapidly (Fig. 22). Note that, owing to the modest mode amplitude, the width of each resonance is modest. Nevertheless, the overlapping resonances produce appreciable transport. Experimental measurements show that, because the resonances differ in different parts of phase space, the threshold for stochastic transport differs in different parts of phase space.[89] The threshold correlates with the destruction of KAM surfaces (Fig. 22); in other words, EP transport becomes large when the orbits become chaotic. Further discussion of these examples appears in Sec. 5 of Todo's review paper.[54]

A single mode of sufficiently large amplitude can also produce stochastic transport. A relatively simple example was analyzed by Konovalov and Putvinskii[91] and Mynick.[90] Consider circulating EPs with $v_\parallel \simeq v$ in a tokamak that also contains a large helical perturbation with toroidal mode number $n = 1$ and poloidal mode number $m = 2$. (Perturbations of this type are produced by tearing modes.). The circulating EPs experience a large curvature drift. The curvature drift can

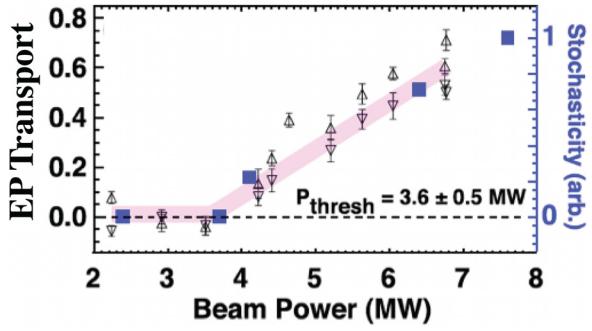

FIG. 22. Stiff beam-ion transport in the presence of multiple Alfvén eigenmodes in the DIII-D tokamak. The abscissa is the injected beam power that drives the instabilities; both the number of modes and their amplitude increases with beam power.[86] The ordinate is the divergence of EP flux from the measured phase-space volume,[87] inferred from a neutral-particle signal. The blue squares represent the fraction of orbits with broken KAM surfaces in the measured phase-space volume. The observed transport threshold occurs when the overlap of multiple resonances causes the destruction of quasi-periodic orbits. Reproduced with permission from Collins *et al.*, Phys. Rev. Lett. **116**, 095001 (2016).[88] Copyright 2016 American Physical Society.

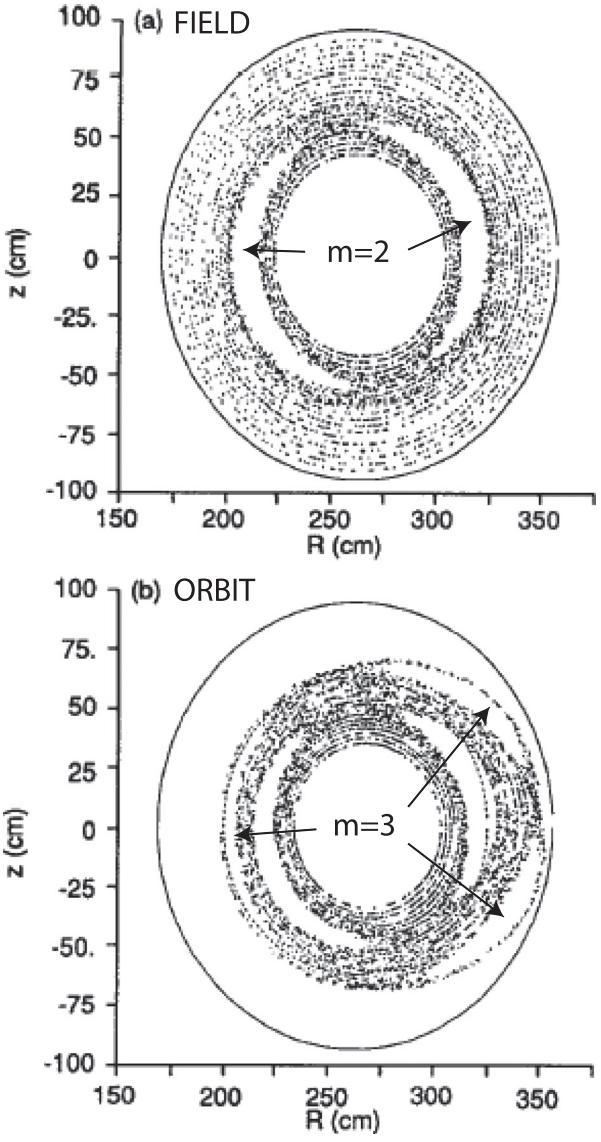

FIG. 23. (a) Poincare plot of magnetic field lines. The axisymmetric field lines are perturbed by an $m = 2$, $n = 1$ perturbation. (b) Poincare plot for a co-passing EP in the same field as (a). The curvature drift creates an additional $m = 3$, $n = 1$ island chain. When the $m = 2$ and $m = 3$ island chains overlap, the orbit becomes chaotic. Reproduced with permission from Mynick, Phys. Fluids B **5**, 1471 (1993).[90] Copyright 2007 AIP Publishing.

be thought of as adding an $n = 0$, $m = 1$ perturbation to a particle orbit that would otherwise follow the field lines. When one plots the Poincare map for the orbit, an $n = 1$, $m = 2 + 1 = 3$ island appears associated with beating between the tearing mode and the curvature drift (Fig. 23). If the mode amplitude and EP energy are modest, the effect on the orbit is negligible. However, when the mode amplitude and EP energy are sufficiently large that the $m = 2$ and $m = 3$ islands begin to overlap, stochasticity ensues. For the example shown in Fig. 23, this occurs when the mode amplitude is doubled.

As predicted, experimental measurements show EP confinement is degraded for large amplitude tearing modes.[3,92–94] The degradation agrees qualitatively with the island overlap theory and quantitatively with numerical calculations.[95] Recent calculations show that the effect on trapped particles is even stronger than the effect on the passing particles of Fig. 23.[96,97] This is not surprising, as trapped particle displacements in tokamaks are even larger than passing-particle orbit shifts.

In the previous examples, the temporal variation of the mode amplitude was gradual; however, in practice, the perturbing fields may rapidly cross a stochastic threshold. When this occurs, a domino effect may occur that causes a sandpile-like avalanche of EP transport, as the overlap of closely spaced modes or the growth of previously stable modes occurs.[98] In these situations, the connection between mode stability and fast-ion gradients causes a complicated interplay between mode amplitude and fast-ion transport that is best treated theoretically by a comprehensive simulation such as the one in Ref. 99. Nevertheless, from the standpoint of EP transport alone, the phenomenon can be understood as another example of enhanced transport when a stochastic threshold is crossed.

Figure 24 shows examples from the spherical tokamak NSTX and the conventional tokamak JT-60U. In both cases, neutral beams inject circulating ions with speeds greater than the Alfvén speed that drive Alfvén eigenmodes unstable. A sequence of repetitive bursts of moderate amplitude ensues [Figs. 24(a) and 24(b)]. At some point, amplitudes grow larger and trigger a major event that involves more toroidal mode numbers at larger amplitudes, called an "avalanche" at NSTX and an "abrupt large-amplitude event" (ALE) at JT-60U. For both devices, in both simulation[99,100] and experiment,[101,102] the avalanches cause EP transport that is an order of magnitude larger than the smaller preceding events [Figs. 24(c)–24(e)]. At an avalanche in NSTX, the pitch of lost fast ions spans a much wider range of values than normal, a signature of chaotic orbits.[103]

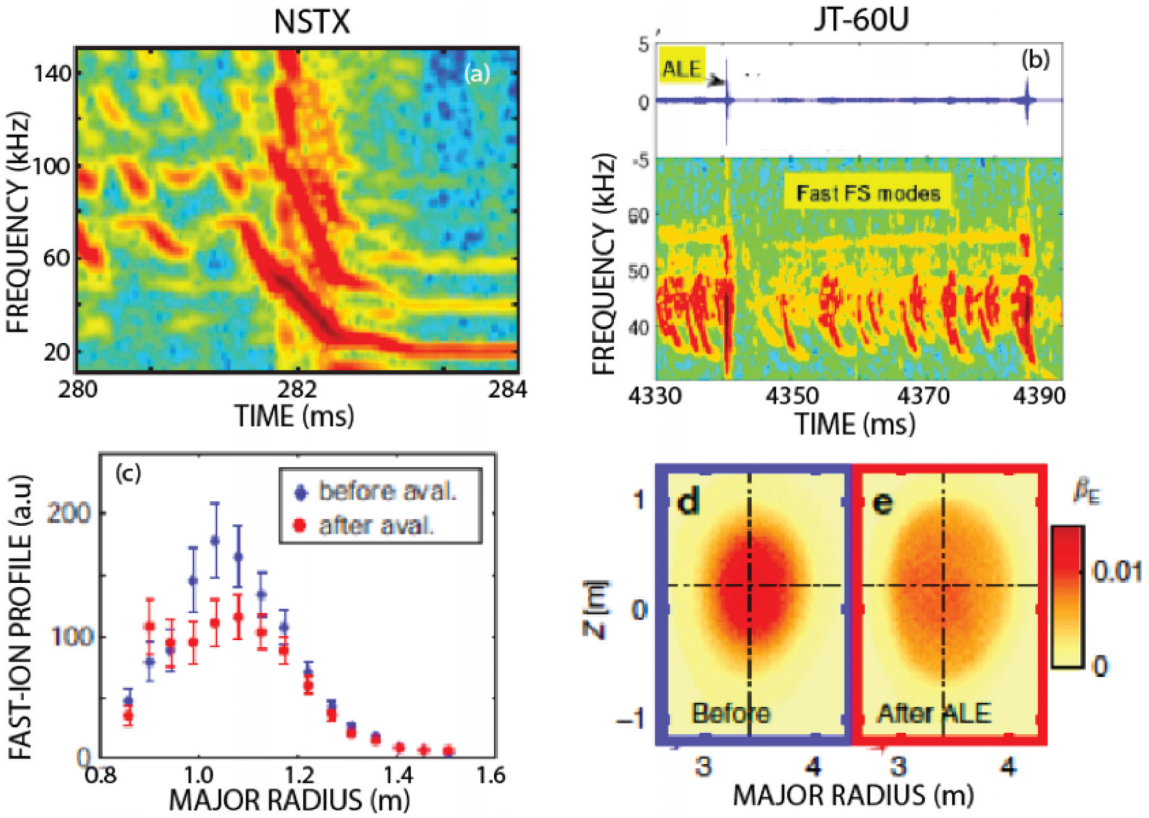

FIG. 24. Examples of avalanche activity in the (left) NSTX and (right) JT-60U tokamaks. (a) Spectrum of magnetic probe signal. An avalanche occurs at 282 ms. (b) Magnetic signal and spectrum. The smaller bursts are "frequency sweeping" events; the event labeled "ALE" is an avalanche. (c) Fast-ion profile inferred from fast-ion D-alpha data before and after an avalanche event. (d) and (e) EP beta before and after an "ALE" as calculated by the hybrid kinetic-MHD code MEGA. NSTX figures reproduced with permission from Podestà *et al.*, Phys. Plasmas **16**, 056104 (2009).[101] Copyright 2009 AIP Publishing. JT-60U spectra reproduced with permission from Bierwage *et al.*, Nucl. Fusion **57**, 016036 (2017).[104] Copyright 2017 International Atomic Energy Agency. JT-60U profile reproduced with permission from Bierwage *et al.*, Nat. Commun. **9**, 3282 (2018).[99] Copyright 2018 Authors, under a Creative Commons CC BY license.

VIII. NONLINEAR EFFECTS

If the perturbation becomes sufficiently large, new resonances are created. These resonances are sometimes called "fractional resonances" because the "integers" in the resonance condition of Eq. (13) now assume rational values such as 1/2 or 1/3. These fractional values occur when the phase of the perturbation is the same after the particle has completed two, three, or more transits of its orbit.[54]

The mathematical origin of these new resonances is easily seen. The nonlinear production of additional resonances was studied by Fibonacci (1170–1250 A.D.) centuries ago. Consider two perturbations of equal amplitude α but different toroidal and poloidal mode numbers m/n and m'/n'. Simply multiplying the terms $\alpha e^{i(m\theta-n\phi)}$ and $\alpha e^{i(m'\theta-n'\phi)}$ gives $\alpha^2 e^{i(m+m')\theta-i(n+n')\phi}$. In addition to the original resonances at m/n and m'/n', a higher-order fraction $(m+m')/(n+n')$ has been created. Note that the higher order fraction is always bounded by the parent fractions. By continuing to multiply perturbations thus produced there results an infinite number of islands produced by any pair. Nevertheless, the KAM[18] theorem guarantees that if the original perturbations are sufficiently small, the sum of all these island widths remains small, so that there are domains in which the original KAM surfaces are distorted but retain their original topology.

The physical origin of these new resonances is also easy to understand. The EP "sees" a wave phase $\Theta = \mathbf{k}\cdot\mathbf{r} - \omega t$. If the wave amplitude is sufficiently large to deflect the equilibrium orbit a distance $\delta\mathbf{r}$, the wave phase is modified by an amount $\mathbf{k}\cdot\delta\mathbf{r}$. This change modifies the original wave-particle resonant interaction and creates additional resonances. The experiment illustrated in Fig. 20 provides a readily understood example. In some cases, the EP orbit passes through two unstable Alfvén eigenmodes of appreciable amplitude. The modes are at different positions in the plasma but the orbit traverses both of them. When that happens, each mode gives the orbit a kick that modifies the phase at the other location. When the phase factor Θ is expanded and the orbital displacement is calculated, in addition to oscillating displacements at the primary mode frequencies ω_1 and ω_2, displacements also occur at the sum and difference frequencies $\omega_1+\omega_2$ and $|\omega_1-\omega_2|$. As expected, when the mode amplitudes are appreciable, losses at the sum and difference frequencies are observed experimentally.[105,106]

A general theory of nonlinear resonances was recently published.[107] In generalized phase-space coordinates X, the equivalent of $\mathbf{k}\cdot\mathbf{r}$ is $\delta X\cdot\nabla_X$. Integration over the unperturbed orbit results in an expansion in Bessel functions whose argument is the phase change. A nonlinear resonance becomes important whenever a phase change is $O(1)$.

A tokamak instability called the energetic-particle-induced geodesic acoustic mode (EGAM) provides an example of this phenomenon. The EGAM is a low-frequency, global electrostatic perturbation of $n=0$, $m=1$ structure that can assume large amplitudes under some conditions. For this instability, the resonance condition reduces to $\omega = m\omega_\theta$. An orbit-following code analyzed the effect on the orbits as a function of mode amplitude. At low amplitude, energy exchange occurred at the usual integer values of m [Fig. 25(a)] but, as the mode amplitude increased, appreciable energy exchange appeared at $m=1/2$ [Fig. 25(c)]. Experimental evidence in support of the phenomenon was found in a loss-detector signal that observed coherent losses at $\omega/2$ in a plasma with a large-amplitude EGAM.[108]

The ASDEX-Upgrade tokamak provides a second example. In this experiment, three-dimensional static field perturbations are superimposed upon the usual axisymmetric tokamak fields. Neutral beams are the source of EPs. Since the perturbing fields are static ($\omega=0$) and μ is conserved, the linear resonance condition [Eq. (13)] is $n\omega_\phi = m\omega_\theta$ for these conditions. For all mode amplitudes, changes in canonical angular momentum P_ϕ are observed at the linear resonances but, at higher amplitude, P_ϕ also changes at fractional resonances (Fig. 26). Measurements with fast-ion loss detectors are consistent with the calculations.[109]

IX. CONCLUSION

For fast ions in magnetic fusion devices, small EP transport is desirable. In the present devices, neutral beams or ion-cyclotron heated ions are used to heat the plasma or provide momentum and current. In a reactor, charged fusion products must transfer their energy to the bulk plasma before escaping; moreover, concentrated losses threaten the integrity of the walls. From the standpoint of fast ions, the large EP orbits are both a benefit and a curse. For nonresonant perturbations, orbit averaging significantly reduces transport to levels well below that of thermal ions. However, the large orbits

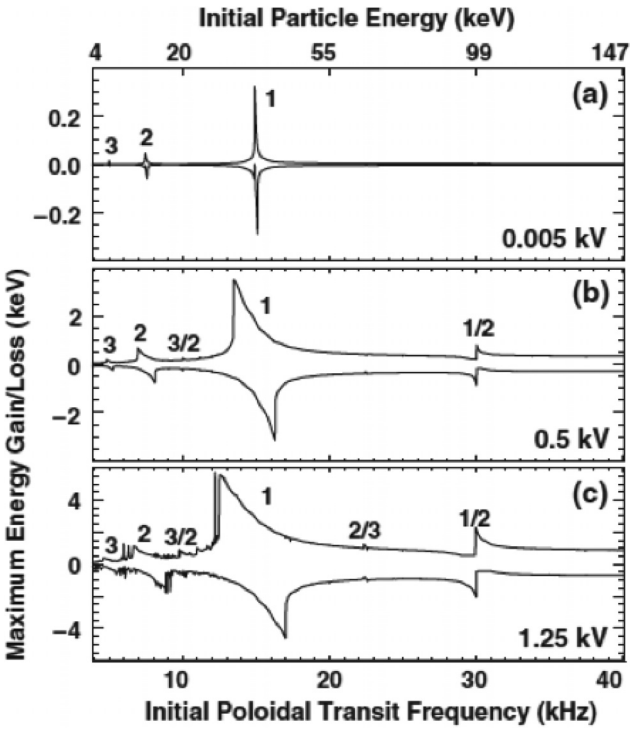

FIG. 25. Minimum and maximum particle energy excursion as a function of the initial poloidal transit frequency $\omega_\theta/(2\pi)$ for various values of the electrical potential of an EGAM of frequency 15 kHz. The numbers beside the peaks represent ω/ω_θ. (a) At low EGAM amplitude, only linear resonances appear. (b) When the EGAM amplitude is 100 times larger, trapping in the fundamental $\omega=\omega_\theta$ resonance causes substantial resonance broadening and a fractional resonance at $\omega/\omega_\theta = 1/2$ becomes apparent. (c) Increasing the amplitude further causes further broadening and the appearance of additional fractional resonances. Conditions taken from a DIII-D experiment. Reproduced with permission from Kramer *et al.*, Phys. Rev. Lett. **109**, 035003 (2012).[108] Copyright 2012 American Physical Society.

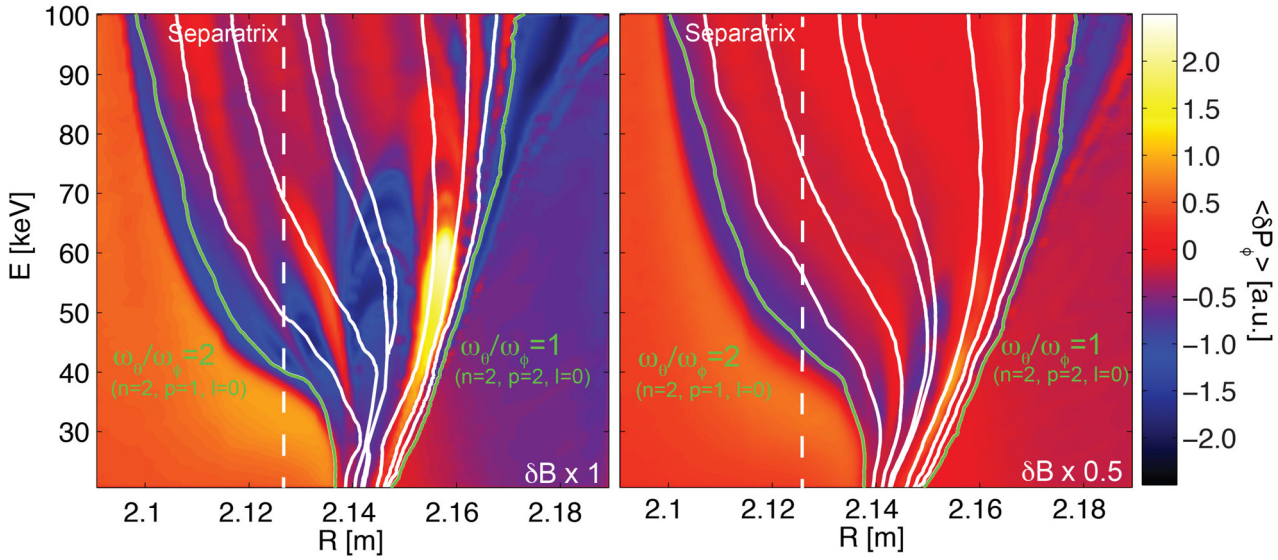

FIG. 26. Appearance of nonlinear resonances near the edge of the ASDEX-Upgrade tokamak in the presence of static perturbing 3D fields with toroidal mode number $n = 2$. The contour map shows the change in toroidal canonical angular momentum for EPs of fixed μ vs major radius and energy. The green lines are the ordinary linear resonances. The white lines indicate nonlinear resonances. (a) Significant changes in P_ϕ occur at nonlinear resonances when the perturbing amplitude is at the experimental value but (b) δP_ϕ is negligible at nonlinear resonances when the amplitude is halved. Reproduced with permission from Sanchis *et al.*, Plasma Phys. Controlled Fusion **61**, 014038 (2019).[109] Copyright 2019 International Atomic Energy Agency.

increase the number of important resonances, enhancing the probability that fast-ion driven instabilities will cause appreciable transport.

For runaway electrons, the situation is reversed: poor confinement is desirable in order to minimize acceleration to high energies and the creation of additional runaways through an avalanche process. Non-resonant orbit averaging inhibits the ability of external perturbations to degrade runaway confinement. On the other hand, resonant interactions with internally excited or externally launched waves might prove useful in minimizing runaway damage.

Although the basic mechanisms of EP transport are known, much remains to be understood. We have treated the perturbations as given when, in truth, EP transport and mode stability are often tightly coupled in a feedback loop (Sec. IV D). For an EP-driven instability, the growth or damping of the wave amplitude depends upon EP gradients, which depend upon the EP transport caused by the mode, which depends upon the mode amplitude. Much remains to be understood and experimentally confirmed about this coupled system. Another artificial aspect of the material presented here is that each perturbation is treated independently when, in practice, different types of perturbations often act concurrently and synergistically on the EP population. The fundamentals presented here are the building blocks of a comprehensive understanding of the EP distribution function.

ACKNOWLEDGMENTS

The many helpful suggestions on the tutorial presentation by students and colleagues are gratefully acknowledged, especially the review committee of E. Bass, C. Collins, X. Du, L. Stagner, and M. Van Zeeland and the figures contributed by L. Sanchis and M. García-Muñoz. A. Bierwage, M. Podestà, and the anonymous referees suggested many improvements to the manuscript. Both W.W.H. and R.B.W. are indebted to the U.S. Department of Energy for decades of support of EP research.

REFERENCES

[1]T. H. Stix, Plasma Phys. **14**, 367 (1972).
[2]T. H. Stix, Nucl. Fusion **15**, 737 (1975).
[3]W. W. Heidbrink and G. J. Sadler, Nucl. Fusion **34**, 535 (1994).
[4]A. H. Boozer, Phys. Plasmas **5**, 1647 (1998).
[5]R. J. Goldston and P. H. Rutherford, *Introduction to Plasma Physics* (Institute of Physics, Philadelphia, 1995), Secs. 10.4–10.5.
[6]R. G. Littlejohn, J. Plasma Phys. **29**, 111 (1983).
[7]J. R. Cary and A. J. Brizard, Rev. Mod. Phys. **81**, 693 (2009).
[8]B. N. Breizman, P. Aleynikov, E. M. Hollmann, and M. Lehnen, Nucl. Fusion **59**, 083001 (2019).
[9]R. B. White, *Theory of Tokamak Plasmas*, 2nd ed. (Imperial College Press, London, 2001).
[10]L.-G. Eriksson and F. Porcelli, Plasma Phys. Controlled Fusion **43**, R145 (2001).
[11]J. M. Finn and R. N. Sudan, Nucl. Fusion **22**, 1443 (1982), Sec. 4.
[12]Y. Hayakawa, T. Takahashi, and K. Yoshiomi, Nucl. Fusion **42**, 1075 (2002).
[13]J. A. Rome, Nucl. Fusion **35**, 195 (1995).
[14]S. J. Zweben, R. L. Boivin, C. Chang, G. W. Hammett, and H. E. Mynick, Nucl. Fusion **31**, 2219 (1991).
[15]F. H. Tenney, "Confinement of energetic alphas in TCT and tritons in PLT," Technical Report No. MATT-1132 (Princeton Plasma Physics Laboratory, 1975).
[16]S. K. P. Tripathi, P. M. Bellan, and G. S. Yun, Phys. Rev. Lett. **98**, 135002 (2007).
[17]P. Helander, C. D. Beidler, T. M. Bird *et al.*, Plasma Phys. Controlled Fusion **54**, 124009 (2012).
[18]A. N. Kolmogorov, in Proceedings of the International Congress on Mathematicians, Amsterdam (1957), Vol. 1, p. 315; V. I. Arnold, Russ. Math. Surv. **18**(5), 9 (1963); J. Moser, Math. Phys. Kl. II 1,1 **Kl**(1), 1 (1962).

[19]R. B. White and M. S. Chance, Phys. Fluids **27**, 2455 (1984).
[20]H. Qin, S. Zhang, J. Xiao *et al.*, Phys. Plasmas **20**, 084503 (2013).
[21]T. G. Northrop, *The Adiabatic Motion of Charged Particles* (Interscience Publishers, New York, 1963).
[22]P. M. Bellan, *Fundamentals of Plasma Physics* (Cambridge University Press, Cambridge, 2006), Sec. 3.3–3.4.
[23]R. J. Goldston, R. B. White, and A. H. Boozer, Phys. Rev. Lett. **47**, 647 (1981).
[24]S. D. Scott, J. F. Lyon, J. K. Munro *et al.*, Nucl. Fusion **25**, 359 (1985).
[25]G. Sadler, P. Barabaschi, E. Bertolini *et al.*, Plasma Phys. Controlled Fusion **34**, 1971 (1992).
[26]R. J. Goldston and H. H. Towner, J. Plasma Phys. **26**, 283 (1981).
[27]H. E. Mynick, Phys. Plasmas **13**, 058102 (2006).
[28]A. Bader, M. Drevlak, D. T. Anderson *et al.*, J. Plasma Phys. **85**, 905850508 (2019).
[29]V. V. Nemov, S. V. Kasilov, W. Kernbichler, and G. O. Leitold, Phys. Plasmas **15**, 052501 (2008).
[30]S. I. Braginskii, *Review of Plasma Physics* (Consultants Bureau, New York, 1965), Vol. 1.
[31]R. D. Hazeltine and J. D. Meiss, *Plasma Confinement* (Addison-Wesley, Redwood City, 1992), Chap. 8.
[32]K. Särkimäki, Nucl. Fusion **60**, 036002 (2020).
[33]H. Matsuura and Y. Nakao, Phys. Plasmas **13**, 062507 (2006).
[34]Z. Guo, C. J. McDevitt, and X.-Z. Tang, Plasma Phys. Controlled Fusion **59**, 044003 (2017).
[35]L. Hesslow, O. Embréus, A. Stahl *et al.*, Phys. Rev. Lett. **118**, 255001 (2017).
[36]C. F. Clauser and R. Farengo, Nucl. Fusion **57**, 046013 (2017).
[37]F. Reif, *Fundamentals of Statistical and Thermal Physics* (McGraw-Hill, New York, 1965), Sec. 15.1.
[38]A. Bovet, A. Fasoli, P. Ricci, I. Furno, and K. Gustafson, Phys. Rev. E **91**, 041101(R) (2015).
[39]G. Spizzo, R. White, M. Maraschek *et al.*, Nucl. Fusion **59**, 016019 (2019).
[40]K. Gustafson, P. Ricci, I. Furno, and A. Fasoli, Phys. Rev. Lett. **108**, 035006 (2012).
[41]M. Podesta, M. Gorelenkova, and R. B. White, Plasma Phys. Controlled Fusion **56**, 055003 (2014).
[42]R. B. White, Commun. Nonlinear Sci. Numer. Simul **17**, 2200 (2012).
[43]A. Bierwage and K. Shinohara, Phys. Plasmas **21**, 112116 (2014).
[44]Y. I. Kolesnichenko, A. Konies, V. V. Lutsenko, and Y. V. Yakovenko, Plasma Phys. Controlled Fusion **53**, 024007 (2011).
[45]S. D. Pinches, V. G. Kiptily, S. E. Sharapov *et al.*, Nucl. Fusion **46**, S904 (2006).
[46]R. B. White, N. Gorelenkov, W. W. Heidbrink, and M. A. Van Zeeland, Plasma Phys. Controlled Fusion **52**, 045012 (2010).
[47]W. W. Heidbrink, Phys. Plasmas **15**, 055501 (2008).
[48]W. Zhang, Z. Lin, and L. Chen, Phys. Rev. Lett. **101**, 095001 (2008).
[49]Y. Zhang, W. W. Heidbrink, S. Zhou *et al.*, Phys. Plasmas **16**, 055706 (2009).
[50]R. B. White, N. N. Gorelenkov *et al.*, Phys. Plasmas **25**, 102504 (2018).
[51]T. O'Neil, Phys. Fluids **8**, 2255 (1965).
[52]R. B. White and V. N. Duarte, Phys. Plasmas **26**, 042512 (2019).
[53]B. N. Breizman and S. E. Sharapov, Plasma Phys. Controlled Fusion **53**, 054001 (2011).
[54]Y. Todo, Rev. Mod. Plasma Phys. **3**, 1 (2019).
[55]L. Chen and F. Zonca, Rev. Mod. Phys. **88**, 015008 (2016).
[56]G. R. Smith and A. N. Kaufmann, Phys. Fluids **21**, 2230 (1978).
[57]F. F. Chen, *Introduction to Plasma Physics and Controlled Fusion* (Plenum Press, New York, 1984), Sec. 2.4.
[58]S. Zhou, W. W. Heidbrink, H. Boehmer *et al.*, Phys. Plasmas **17**, 092103 (2010).
[59]S. Zhou, W. W. Heidbrink, H. Boehmer *et al.*, Phys. Plasmas **19**, 055904 (2012).
[60]S. Zhou, W. W. Heidbrink, H. Boehmer *et al.*, Phys. Plasmas **18**, 082104 (2011).
[61]A. B. Rechester and M. N. Rosenbluth, Phys. Rev. Lett. **40**, 38 (1978).
[62]C. W. Barnes and J. D. Strachan, Nucl. Fusion **22**, 1090 (1982).
[63]H. E. Mynick and J. D. Strachan, Phys. Fluids **24**, 695 (1981).
[64]C. W. Barnes, "Studies of runaway electron transport in PLT and PDX," PhD thesis (Princeton University, 1981).
[65]G. Fiksel, B. Hudson *et al.*, Phys. Rev. Lett. **95**, 125001 (2005).
[66]Y. I. Kolesnichenko, V. V. Lutsenko, R. B. White, and Y. V. Yakovenko, Phys. Plasmas **5**, 2963 (1998).
[67]Y. I. Kolesnichenko, V. V. Lutsenko, R. B. White, and Y. V. Yakovenko, Nucl. Fusion **40**, 1325 (2000).
[68]S. K. Nielsen, M. Salewski, H. Bindslev *et al.*, Nucl. Fusion **51**, 063014 (2011).
[69]C. M. Muscatello, W. W. Heidbrink, Y. I. Kolesnichenko *et al.*, Plasma Phys. Controlled Fusion **54**, 025006 (2012).
[70]B. Geiger, M. Garcia-Munoz, R. Dux *et al.*, Nucl. Fusion **54**, 022005 (2014).
[71]J. Rasmussen, S. K. Nielsen, M. Stejner *et al.*, Nucl. Fusion **56**, 112014 (2016).
[72]M. Weiland, B. Geiger, A. Jacobsen *et al.*, Plasma Phys. Controlled Fusion **58**, 025012 (2016).
[73]D. Liu, W. W. Heidbrink *et al.*, Nucl. Fusion **58**, 082028 (2018).
[74]R. B. White, R. J. Goldston, K. McGuire *et al.*, Phys. Fluids **26**, 2958 (1983).
[75]W. W. Heidbrink, M. E. Austin, R. K. Fisher *et al.*, Plasma Phys. Controlled Fusion **53**, 085028 (2011).
[76]L. Chen, Phys. Plasmas **1**, 1519 (1994).
[77]P. Beiersdorfer, R. Kaita, and R. J. Goldston, Nucl. Fusion **24**, 487 (1984).
[78]J. D. Strachan, B. Grek, W. Heidbrink *et al.*, Nucl. Fusion **25**, 863 (1985).
[79]K. Nagaoka, M. Isobe, K. Toi *et al.*, Phys. Rev. Lett. **100**, 065005 (2008).
[80]M. García-Muñoz, N. Hicks, R. Van Voornveld *et al.*, Phys. Rev. Lett. **104**, 185002 (2010).
[81]R. B. Zhang, G. Y. Fu, R. B. White, and X. G. Wang, Nucl. Fusion **55**, 122002 (2015).
[82]X. Chen, M. E. Austin, R. K. Fisher *et al.*, Phys. Rev. Lett. **110**, 065004 (2013).
[83]X. Chen, W. W. Heidbrink, G. J. Kramer *et al.*, Nucl. Fusion **53**, 123019 (2013).
[84]C. T. Hsu and D. J. Sigmar, Phys. Fluids B **4**, 1492 (1992).
[85]Y. Todo, M. A. Van Zeeland, and W. W. Heidbrink, Nucl. Fusion **56**, 112008 (2016).
[86]W. W. Heidbrink, C. S. Collins, M. Podesta *et al.*, Phys. Plasmas **24**, 056109 (2017).
[87]W. W. Heidbrink, C. S. Collins, L. Stagner *et al.*, Nucl. Fusion **56**, 112011 (2016).
[88]C. S. Collins, W. W. Heidbrink, M. E. Austin *et al.*, Phys. Rev. Lett. **116**, 095001 (2016).
[89]C. S. Collins, W. W. Heidbrink, M. E. Austin *et al.*, Nucl. Fusion **57**, 086005 (2017).
[90]H. E. Mynick, Phys. Fluids B **5**, 1471 (1993).
[91]S. V. Konovalov and S. V. Putvinskii, Sov. J. Plasma Phys **14**, 461 (1988).
[92]C. B. Forest, J. R. Ferron, T. Gianakon *et al.*, Phys. Rev. Lett. **79**, 427 (1997).
[93]M. García-Muñoz, P. Martin, H.-U. Fahrbach *et al.*, Nucl. Fusion **47**, L10 (2007).
[94]M. Gobbin, L. Marrelli, H. U. Fahrbach *et al.*, Nucl. Fusion **49**, 095021 (2009).
[95]E. M. Carolipio, W. W. Heidbrink, C. B. Forest, and R. B. White, Nucl. Fusion **42**, 853 (2002).
[96]W. W. Heidbrink, L. Bardoczi, C. S. Collins *et al.*, Nucl. Fusion **58**, 082027 (2018).
[97]L. Bardóczi, M. Podestà, W. W. Heidbrink, and M. A. Van Zeeland, Plasma Phys. Controlled Fusion **61**, 055012 (2019).
[98]H. L. Berk, B. N. Breizman, J. Fitzpatrick, and H. V. Wong, Nucl. Fusion **35**, 1661 (1995).
[99]A. Bierwage, K. Shinohara, Y. Todo *et al.*, Nat. Commun. **9**, 3282 (2018).
[100]M. Podestà, M. Gorelenkova, E. D. Fredrickson, N. N. Gorelenkov, and R. B. White, Nucl. Fusion **56**, 112005 (2016).
[101]M. Podestà, W. W. Heidbrink, D. Liu *et al.*, Phys. Plasmas **16**, 056104 (2009).
[102]M. Ishikawa, M. Takechi, K. Shinohara *et al.*, Nucl. Fusion **45**, 1474 (2005).
[103]D. S. Darrow, N. Crocker, E. D. Fredrickson *et al.*, Nucl. Fusion **53**, 013009 (2013).
[104]A. Bierwage, K. Shinohara, Y. Todo *et al.*, Nucl. Fusion **57**, 016036 (2017).
[105]X. Chen, G. J. Kramer, W. W. Heidbrink *et al.*, Nucl. Fusion **54**, 083005 (2014).
[106]W. W. Heidbrink, E. A. D. Persico, M. E. Austin *et al.*, Phys. Plasmas **23**, 022503 (2016).
[107]L. Chen and F. Zonca, Plasma Sci. Technol. **21**, 125101 (2019).
[108]G. J. Kramer, L. Chen, R. K. Fisher *et al.*, Phys. Rev. Lett. **109**, 035003 (2012).
[109]L. Sanchis, M. Garcia-Munoz, A. Snicker *et al.*, Plasma Phys. Controlled Fusion **61**, 014038 (2019).